NGC 4314. I. VISIBLE AND SHORT-WAVELENGTH INFRARED SURFACE PHOTOMETRY OF THE NUCLEUS AND BAR

G. F. BENEDICT
McDonald Observatory, University of Texas, Austin, Texas 78712

J. L. HIGDON
Astronomy Department, University of Texas, Austin, Texas 78712

E. V. TOLLESTRUP
Center for Astrophysics, Harvard–Smithsonian, Cambridge, Massachusetts 02138

J. M. HAHN
Department of Physics, Notre Dame University, Notre Dame, Indiana 46556

P. M. HARVEY
Astronomy Department, University of Texas, Austin, Texas 78712
Received 7 October 1991; revised 13 November 1991

ABSTRACT

We present *BVI* (TI CCD) and *JHK* (University of Texas IR Camera) surface photometry of NGC 4314, an SB(rs)ap anemic spiral with a nuclear ring containing recent star formation. The shortwave IR (SWIR) frames reveal a nuclear bar of length 2 arcsec at P.A. = 0°. The nuclear ring and associated dust have been detected in all SWIR color indices. We have detected a nuclear spiral in the visible and SWIR just exterior to the ring. We find extremely low amplitude spiral-shaped deficits in the stellar distribution in the SWIR in this same region. We attribute these to dust, since CO is detectable at or near these locations. Average minor-axis profiles show this galaxy to have a nuclear bulge obeying the de Vaucouleurs $r^{1/4}$ law for values of $2 < r < 7$ arcsec. Away from the dust lanes and patches, the bar is shown to have an exponential cross section. We find that the extinction characteristics of a dusty region in the bar are similar to those of dust in our Galaxy. We have determined extinction and scattering characteristics of dust near the sites of recent star formation in the nuclear ring. Because of scattering, the $I - J$ color index best maps dust near the nuclear ring. Unsharp masking techniques reveal structure all along the bar. The dust lanes associated with the bar terminate well before the ends of the bar and appear to turn back toward the galaxy center. We argue that some of the structure in the bar can be explained as resonance phenomena. We also interpret multiple peaks within previously published CO spectra as gas streaming along the dust lanes in the bar. Shocks at the intersection points of the gas in the bar dust lanes and the gas in the rotating inner ring are a likely explanation for the ring of star formation. We discuss several mechanisms capable of forming and maintaining the nuclear spiral found just outside the nuclear ring. No one mechanism compellingly explains this spiral.

1. INTRODUCTION

NGC 4314, an SB(rs)ap galaxy (de Vaucouleurs *et al.* 1976), contains one of the larger nuclear rings of active star formation found in a barred galaxy. Moreover, NGC 4314 has one of the few nuclear rings found in early type galaxies. Though large, the nuclear ring is still small enough to study with new IR detector arrays, which are often limited in their areal coverage. In addition, the bar of NGC 4314 contains rather peculiarly shaped dust lanes, somewhat similar to those found in a few other barred galaxies (cf. NGC 1433, Buta 1986), but dissimilar to the long, narrow lanes (e.g., NGC 1300) predicted by shock models (Roberts *et al.* 1979). This class of galaxy provides a smoother and simpler environment within which to study these dust lanes and the near-nucleus star formation.

We wish to explore the relationships between the gas, the dust, the stars, and the star-forming regions in the galaxy. An ultimate goal is to identify and characterize all of the major organizational components of NGC 4314. These components might include: the nuclear bulge or spheroid, a nuclear bar, the bar, a disk, a lens, nuclear and outer spiral arms, and nuclear, inner, and outer rings. While NGC 4314 does not have an active galactic nucleus (AGN), the interaction of some of its components may bear on the interesting issue of fueling AGNs, since bars and nuclear rings are possible factors (Shlosman *et al.* 1990).

Previous surface photometry of NGC 4314 includes the low-resolution blue and red photographic photometry of Lynds *et al.* (1973) and the *UBV* surface photometry (FWHM = 2.7 arcsec) of the inner 40 arcsec of Benedict (1980). The major conclusion of the latter work was that the locus of new star formation is a ring, broken in two locations by dust. The ring is relatively complete when seen in Q, the reddening-free parameter derived from *UBV* photometry. Pogge (1989) presents a Hα map of the nucleus with about 2 arcsec resolution, which shows a ring-like distribution. He claims that 94% of the observed Hα is associated with H II regions. The gaps in his ring match those found by Benedict (1980).

Garcia-Barreto *et al.* (1989, 1990, hereafter referred to as GB I and GB II) have mapped the nucleus at 2, 6, and 20 cm

 0004-6256/92/030757-27$00.90

at the VLA (3.5 arcsec beam) and in CO (2-1) at the IRAM (12.5 arcsec beam). They find a ring structure in all radio continuum wavelengths, although the ring is much fainter in the angular range 190° < P.A. < 270°. They also report that NGC 4314 is H I deficient, based on Arecibo 21 cm observations. This latter result agrees nicely with van den Bergh's (1976) classification of NGC 4314 as anemic. He postulates that all anemic galaxies are hydrogen deficient (van den Bergh 1991).

In this paper, when we speak of *the ring*, we are referring to the nuclear ring structure shown in Benedict, Pogge, and GB II. As we shall see, the environment of this nuclear ring has many attributes normally associated with spiral structure and in this context we shall use the term *nuclear spiral*, as distinct from the *outer spiral*, which is the spiral structure visible on Palomar Observatory-National Geographic Sky Survey (POSS) prints.

Wakamatsu & Nishida (1980, hereafter referred to as WN) present a Hα rotation curve for the inner 10 arcsec and estimate an inclination of $i = 30°$. They presume solid-body rotation for $r \leqslant 10$ arcsec. Assuming trailing arms, the southwest side is nearest to us.

IRAS data show this galaxy to be normal in the FIR. By the criteria of Soifer *et al.* (1989), NGC 4314 is cold, e.g., $F(25\mu)/F(60\mu) < 0.17$. It is lukewarm according to the precepts discussed by Dresel *et al.* (1990) since $F(100\mu)/F(60\mu) = 2.02$, which is slightly above their cutoff of 2.00. A virtually featureless near-IR (effective wavelength of 825 nm) photograph appears in Elmegreen (1981).

Why do surface photometry? First, we are motivated by the sometimes naive assumption that the distribution of light maps the distribution of stars. Multibandpass surface photometry allows identification of stars by spectral class, which then maps into stellar age. Second, it provides information on dust location and characteristics. In addition, shortwave-IR (SWIR) surface photometry allows a look through the dust, providing information on the distribution of the oldest and most-evolved stars. Moreover, SWIR surface photometry indicates the location of the "most effective" (largest optical depth) dust. Finally, surface photometry allows us to identify H II regions, sites of recent massive star formation.

This is the first paper in a series exploring the morphology and dynamics of NGC 4314. This paper will extend previous photometric efforts in both wavelength and areal coverage by presenting *B*, *V*, and *I* surface photometry over the inner 3 arcmin and *J*, *H*, and *K* shortwave IR (SWIR) surface photometry over the inner 40 arcsec. Better knowledge of the nuclear morphology of NGC 4314 will come with higher-resolution *HST* data (Paper II). A better understanding of the physical conditions producing this morphology will come from detailed knowledge of the dynamics of gas within the galaxy. We will report on interferometric CO observations in Paper III.

The areal coverage of the present data precludes us from saying anything definitive about the disk or lens component or the weak outer spiral arms. These components will be explored in the future. As a final point, most nuclear spirals occur in late type galaxies, which contain much gas and dust. Does the gas and dust supporting new star formation in this early type galaxy come from mass loss from evolving stars or infall from an external source? An answer to this question must, again, wait on future observations.

In Sec. 2 we will describe the instrumentation and observations, and in Sec. 3 the reductions and photometric calibrations. We will discuss in Sec. 4 the internal and external errors. Section 5 presents these data as luminosity and color profiles, and as surface magnitude and color maps. We present detailed examinations and our interpretations of the maps in Sec. 6, investigate the morphological and photometric properties of the dust associated with the bar and with the nuclear ring in Sec. 7, and offer models of some of the photometric components of the galaxy in Sec. 8. The GB CO velocities, discussed qualitatively in Sec. 9, give us some preliminary insight into the star formation process. Also in this section we explore possible kinematic explanations for the nuclear spiral and the radially symmetric structure in the bar. In Sec. 10, we offer a preliminary overview of the several physical processes capable of producing and maintaining the morphology of NGC 4314. Finally, in Secs. 11 and 12 we present conclusions and discuss future work.

In this paper we assume that 1 arcsec = 50 pc, which follows from an adopted distance of 10 Mpc (extensively discussed in GB II).

2. OBSERVATIONS

Our first set of visual observations was obtained with an RCA CCD on the McDonald Observatory 0.8 m telescope during 10–15 May 1988 (observer, M. Frueh). The image scale was 0.57 arcsec/pixel. The filters used included Johnson *B* and *V* and Kron–Cousins I. The seeing was measured to be 1.9 arcsec FWHM.

Unhappy with the 50 electron readout noise in the RCA device, we obtained a second set of visual observations using a TI CCD (22 electron readout noise) on the McDonald Observatory 0.8 m telescope during 1–2 April 1989 (observer, J. Higdon). This chip and telescope combination (using on-chip 2×2 summation) produces an image scale identical to that of the RCA device, i.e., 0.57 arcsec/pixel. The same filter set was used for these observations as those from May 1988. Exposures totalled 30 min in each bandpass. The seeing was measured (using the point-spread function routines in IRAF) on the same star within each frame. For these observations the seeing was characterized by the following FWHM: *B*, 1.58; *V*, 1.70; and *I*, 1.76 arcsec.

To determine sky levels within the CCD frames, one of us (J. Higdon) secured drift scans across NGC 4314 with the L2 photometer (EMI 9658 R, cooled with a dry ice cold box). These observations were obtained on the McDonald Observatory 0.9 m telescope on the nights of 4–5 March 1989 with an aperture of 32 arcsec diameter. We used 30 scans in *B*, 35 scans in *V*, and 24 scans in I to sample the night sky out to 11 arcmin on either side of the center of NGC 4314.

The SWIR observations were secured with the University of Texas IR Array Camera (Joy *et al.* 1988) used on the McDonald Observatory 2.7 m on 28 February 1988 (P. Harvey and E. Tollestrup, observers). The resulting image scale is 1.35 arcsec/pixel. Total on-source integration times were 720 s for *J* (1.25 μm) and *H* (1.65 μm), and 800 s for *K* (2.2 μm). Observations were taken in the following sequence: 3 sky, 6 galaxy, 3 sky, 6 galaxy, and 3 sky. The *J* filter was from Barr Associates and the *H* and *K* filters were from a standard OCLI (Optical Coatings Laboratory Inc.) Astronomical IR filter set. The seeing was estimated from the standard stars to be about 2 arcsec FWHM.

3. REDUCTIONS AND CALIBRATIONS

All reductions were carried out with IDL and IRAF. For the CCD data we first removed the bias from the raw frames. No significant dark current was detected in several hours of dark exposure, so no dark frames were subtracted. The frames were flattened by a flat field made in the following manner: we combined 20 dome flats with "night sky flats," which are several 5–10 min observations of randomly chosen blank regions near the galaxy. The night sky flats were then median filtered to remove stars and then heavily smoothed. These flats were then used to correct the dome flats for nonuniform illumination and color mismatch with the night sky. Finally, bad columns were replaced via linear interpolation, the cosmic ray events removed by an adaptive filtering process, and the sky levels determined from the drift scans.

The IR Array Camera data have had the sky flux removed via sky frames (a blank field several arcmin away from the galaxy), and have been flat fielded with flats developed from these same sky frames. For each color, the series of exposures were registered, stacked, and averaged. Pixels with much higher dark current or much lower response were flagged before registration and not included in the average. Although the SWIR frames covered an 81×86 arcsec area, only the inner 30×30 arcsec were used due to poor flat fielding outside that area.

3.1 Photometric Calibrations

We calibrated the RCA CCD data using observations of *BVRI* standard stars in M67 (Schild 1983). We next calibrated the TI CCD frames using synthetic aperture photometry of NGC 4314 abstracted from the RCA CCD frames. This aperture photometry was from the brightest part of the galaxy and therefore presumably least affected by errors in sky subtraction. The final sky values for the TI frames were derived from the drift scan data. *BVI* standard stars (Landolt 1983) were observed and used to reduce the drift scans to the Johnson and Kron–Cousins systems. In summary, all the *B*, *V*, and *I* results presented in this paper come from the TI data, which was calibrated by comparison with the RCA frames, and which had the sky determined from drift scans.

To calibrate the IR Array Camera data, we used three *JHK* standard stars from Elias *et al.* (1982): SJ9514, SJ9524, and SJ9529.

3.2 Positional Calibrations

For the convenience of future observers and to facilitate the generation of x-ray, radio, and IR overlay maps, we list the position of the nucleus of NGC 4314 and 11 stars contained in the TI CCD field of view (Table 1). The stars are identified in Fig. 1. These astrometric positions were produced with the PDS microdensitometer-based astrometry system developed by Benedict & Shelus (1978). To establish an astrometric grid, thirty SAO reference stars were measured on the Palomar Observatory Sky Survey E plate. This grid was then used to derive a right ascension and declination for the 11 stars seen in the TI CCD field of view. We then used AIPS to establish an astrometric grid for each grey scale map. The average residual resulting from this grid mapping was 0.15 arcsec.

The *J*, *H*, and *K* frames were subsampled and registered to the *B*, *V*, and *I* frames using IRAF. Since there were no positional reference stars in the smaller IR frames, we used the nucleus of the galaxy as the registration point. We iteratively shifted the SWIR image, formed a color index map, visually inspected this map and then shifted again. Misregistrations of 0.1–0.2 pixel were easily detected in the color index maps as asymmetric shadings around the nuclear peak.

All positions in this paper are equinox 2000.0.

4. INTERNAL AND EXTERNAL ERRORS

Table 2 presents internal errors for *B*, *V*, *I*, *J*, *H*, and *K* calculated assuming Poisson statistics. The derived sky levels and uncertainties are also tabulated.

We are able to assess external errors only for the *B* and *V* bandpasses. The *B* and *V* integrated magnitudes agree reasonably well with Benedict (1980) and Vorontsov-Vel'yaminov *et al.* (1972), as shown in Fig. 2. Average *B* and *V* surface magnitudes, derived from synthetic aperture photometry, are compared in Fig. 3, where the brightest surface magnitude for both colors is at $r = 1$ arcsec (with a 1 arcsec spacing between points). We ascribe the large differences for $r \leqslant 3$ arcsec to the seeing differences between the Benedict (1980) and the more recent dataset; the present study is characterized by better seeing. The slope of the fit line for both colors is constrained to be unity. There are apparent

TABLE 1. Stars in the vicinity of NGC 4314.

	R.A. (2000.0)			Dec.								
Identification	h	m	s	d	m	s	*V*	σ	*B* − *V*	σ	*V* − *I*	σ
1	12	22	34.68	29	53	14.0	14.77	0.01	0.51	0.01	0.60	0.01
2	12	22	36.46	29	54	26.7	14.94	0.01	0.78	0.02	0.88	0.01
3	12	22	38.54	29	54	13.2	19.71	0.02	0.83	0.04	2.29	0.02
4	12	22	36.79	29	55	38.1	19.99	0.02	1.51	0.04	—	—
5	12	22	28.95	29	54	49.4	19.56	0.02	0.44	0.04	−0.11	0.02
6	12	22	26.30	29	55	6.5	14.04	0.01	0.37	0.01	0.81	0.01
7	12	22	24.66	29	54	35.2	17.03	0.03	0.52	0.01	0.58	0.01
8	12	22	23.90	29	53	55.2	19.20	0.02	0.76	0.03	—	—
9	12	22	33.19	29	52	9.3	20.15	0.02	1.17	0.04	1.69	0.03
10	12	22	35.76	29	52	1.4						
11	12	22	29.61	29	52	38.5						
Nucleus	12	22	31.97	29	53	44.1						

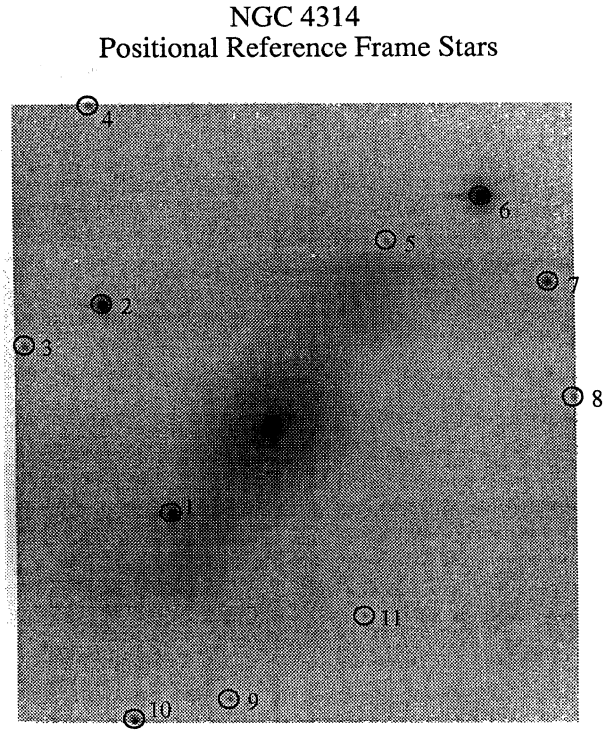

FIG. 1. Finding chart for astrometric reference stars. Positions, magnitudes, and colors are presented in Table 1. North is at top, east to the left.

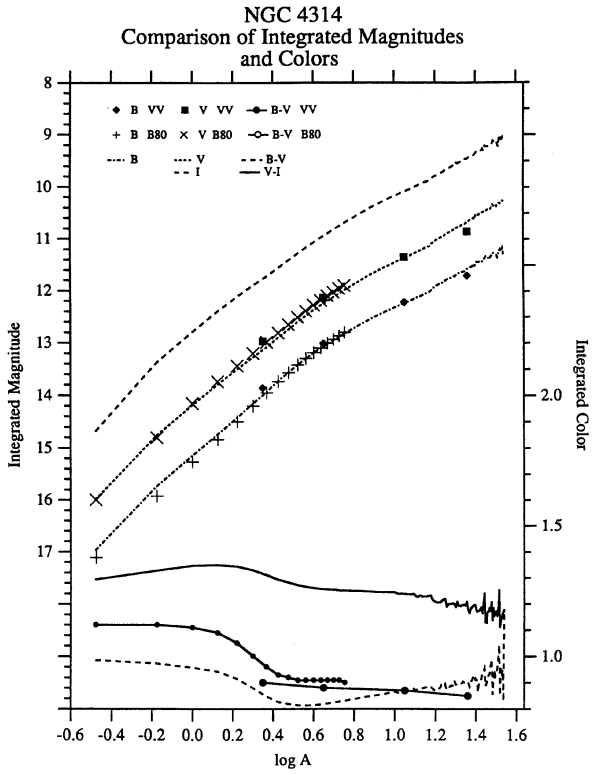

FIG. 2. Comparisons among previous aperture photometry (VV = Vorontsov-Vel'yaminov *et al.* 1972), previous synthetic aperture photometry (B80 = Benedict 1980), and synthetic aperture photometry from the present study.

small zero-point differences.

No previous J, H, and K observations have been located in the literature for this galaxy. As a consistency check, we note that the average nuclear colors match those found by Frogel (1985) for many Sc galaxies. Also, NGC 4314 nuclear surface $V-K$ values agree with those found for the nucleus of M31 by Mould *et al.* (1989).

TABLE 2. Internal errors as a function of surface magnitude.

Surface magnitude	$\sigma(B)$	$\sigma(V)$	$\sigma(I)$	$\sigma(J)$	$\sigma(H)$	$\sigma(K)$
14					0.03	0.04
15				0.02	0.05	0.04
16			0.004	0.02	0.12	0.10
17		0.006	0.006	0.02	0.30	0.30
18	0.010	0.010	0.011	0.04		
19	0.018	0.017	0.019	0.10		
20	0.032	0.032	0.034			
21	0.064	0.063	0.069			
22	0.139	0.136	0.153			
23	0.334	0.329	0.374			

B(night sky) $= 22.78 \pm 0.04$
V(night sky) $= 21.13 \pm 0.02$
I(night sky) $= 18.52 \pm 0.02$

Notes to TABLE 2
Values are magnitudes per square arcsec.
Reduce σ by factor of 2 for detailed profiles.
Reduce σ by factor of $\sqrt{8}$ for average profiles.

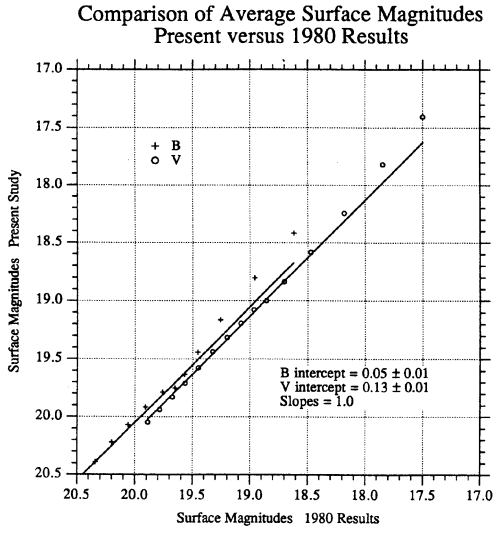

FIG. 3. Comparison of average surface magnitudes within $r < 18$ arcsec. We compare the present study with results from Benedict (1980).

5. THE DATA

We shall present these data as surface magnitude and color maps, contour maps, luminosity and color profiles, and tables. In many cases there will be two sets of derived data, one for the full TI CCD frame (henceforth called the *outer frame*) and one corresponding to the smaller areal coverage of the IR Array Camera (called the *inner frame*). We will point out interesting features within these representations, but refrain from interpretation until Sec. 6. For some of the profile plots we have corrected the colors and magnitudes for extinction within our galaxy. We have assumed $A(B) = 0.08$, $E(B-V) = 0.02$ (Burstein & Heiles 1984), and have derived $A(V) = 0.06$, $A(I) = 0.03$, $A(J) = 0.02$, $A(H) = 0.015$, $A(K) = 0.01$, using the reddening curve of Scheffler & Elsasser (1987). Corrected magnitudes and colors will be subscripted, e.g., $(B-V)_0$. No corrections due to reddening from our Galaxy have been applied to any of the surface magnitude and color index maps.

5.1 Surface Magnitude and Color Maps

Grey scale encoded surface magnitude and color index maps of the full CCD field of view and of the nuclear region are presented in Figs. 4 and 5 [Plates 57 and 58] (outer frame) and Figs. 6 and 7 [Plates 59–61] (inner frame). We first discuss the outer frame. Figure 4(a), which is a B surface magnitude per square arcsec map (hereafter, μ_B), and Fig. 5(a), a $B-V$ surface color map (μ_{B-V}), will serve to introduce us to the major structural components of NGC 4314. These include a strong bar containing the end-of-bar brightenings often seen in SB/0 SBa galaxies (e.g., NGC 4548 and 4596; Benedict 1976). Note the weak outer arms with no obvious star formation sites, consistent with the anemic classification of van den Bergh (1976). The bar contains dust lanes and patches (easily seen in Fig. 5) and appears embedded in a lens in all bandpasses (Fig. 4). Finally, there are the nuclear spiral and ring first discussed by Sandage (1961). The $B-V$ color index map [Fig. 5(a)] shows the region interior to the ring to be the reddest. The bar has a uniform color except in the dust lanes and patches. The nuclear ring has the bluest colors. The nuclear spiral, just exterior to the nuclear ring, has colors midway between the nuclear ring and the bar. The bright stars show that even slight seeing differences can cause spurious color indices in regions of rapid brightness change. Note the blue knot at the bar end to the NW (No. 5, Fig. 1). As this object is possibly unassociated with NGC 4314, we discuss it in Appendix I.

The μ_{V-I} color index image [Fig. 5(b)] shows the same features seen in μ_{B-V}. The meandering, seemingly disorganized dust lanes and patches are better delineated since the S/N in μ_V and μ_I is greater than that in the μ_B data. We have dubbed the large dust patch to the SE (R.A. = $12^h\ 22^m\ 32.8^s$, Dec. = $+29°53'22''$) the "dust bowl." The broadening of the inner spiral arms to the southwest and northeast is more apparent in μ_{V-I}. Again, object No. 5 is shown to be much bluer than the bar. Neither our frame size nor exposure times permit accurate, detailed photometry of the faint, outer spiral arms of this galaxy.

We turn now to the inner frame. The intricate morphology of the nuclear region warrants larger scale displays. Surface magnitude maps for all bandpasses are displayed in Fig. 6. In μ_B the nucleus resembles a spiral with a nuclear bar oriented along the same axis as the outer bar. The two brightest H II regions east (R.A. = $12^h\ 22^m\ 32.45^s$, Dec. = $+29°53'45''$) and south (R.A. = $12^h\ 22^m\ 31.95^s$, Dec. = $+29°53'39''$) of the center are designated knot *A* and *B* by WN (see also Fig. 28). Dust and H II regions are much less prominent in μ_I, and have apparently disappeared in μ_J.

Various color indices are displayed in Fig. 7(a). The μ_{B-V} image shows that the reddening interior to the ring defined by the H II regions is rather uniform. Note that the defective columns that pass through the steep gradients near the nucleus could not always be adequately corrected [the two bright linear features just E of the nucleus in Fig. 7(a), $B-V$]. Colors along the nuclear spiral arms get redder as the arms get further away from the stellar nurseries in the ring. In μ_{V-I} the dust lanes interior to the ring are resolved into clumps. Blue, newer stars delineate an apparent spiral pattern exterior to the ring of H II regions. The nucleus appears slightly bluer, and is probably caused by point-spread function mismatch and the steep gradients found within the inner 2 arcsec. The μ_{V-I} map also contains a bad column just E of nucleus.

We now turn to the first SWIR color index map, μ_{I-J}. As we shall discuss below, dust is most prominent in this index. To best display this we have inverted the grey scale mapping and expanded the physical scale somewhat [Fig. 7(b)]. Dust lanes can be traced to within 2.5 arcsec of the nucleus at P.A. = 20° and 200° in μ_{I-J}. Note that the nuclear bar seen in μ_B may be partially an artifact due to the masking effect of the dust lanes. Note also [Fig. 7(a)] that nuclear blueing is always seen when forming color indices across instruments and is probably caused by seeing differences. In contrast the nucleus is redder in all SWIR color indices.

The μ_{V-K} map [Fig. 7(a)] is similar to μ_{I-J}. Again, there is evidence for a color progression in the nuclear spiral arms with the bluer stars nearest to the ring while the redder stars are farther out along the arms and away from the ring. The arms also widen along a clockwise direction. In each color index map involving optical images, the bluest regions are positionally coincident with the H II regions mapped by Pogge (1989). This is not the case for the purely SWIR indices; no H II regions are readily apparent. However, it is evident that the ring and associated dust are detected in all the SWIR indices, albeit weakly. We have increased the contrast on all the SWIR color index maps to exaggerate the small color differences.

5.2 Contour Maps

Contour maps are useful for determining shape and orientation parameters. In addition they provide clear detection threshold information. Figure 8 presents the CCD data for regions of complete overlap between μ_B, μ_V, and μ_I. From these we determine a bar position angle, P.A. = 148°. Note the "islands" in the bar in μ_V and the perturbed contours at the dust bowl in the SE bar in μ_B. The outer bar contours are boxlike.

The bar and nucleus μ_B, μ_V, μ_I, μ_J, μ_H, and μ_K contour maps (Fig. 9) cover only the inner 34×36 arcsec. The reduced signal to noise for μ_K is evident. Note the north-south nuclear elongation, prominent in the SWIR frames. The nuclear elongations seen in the μ_J, μ_H, and μ_K contour maps are not likely to be telescope drift. The drift would have to be constant in rate and direction during the hour or so required to obtain the SWIR observations but not during the observations of the standard stars, which were observed

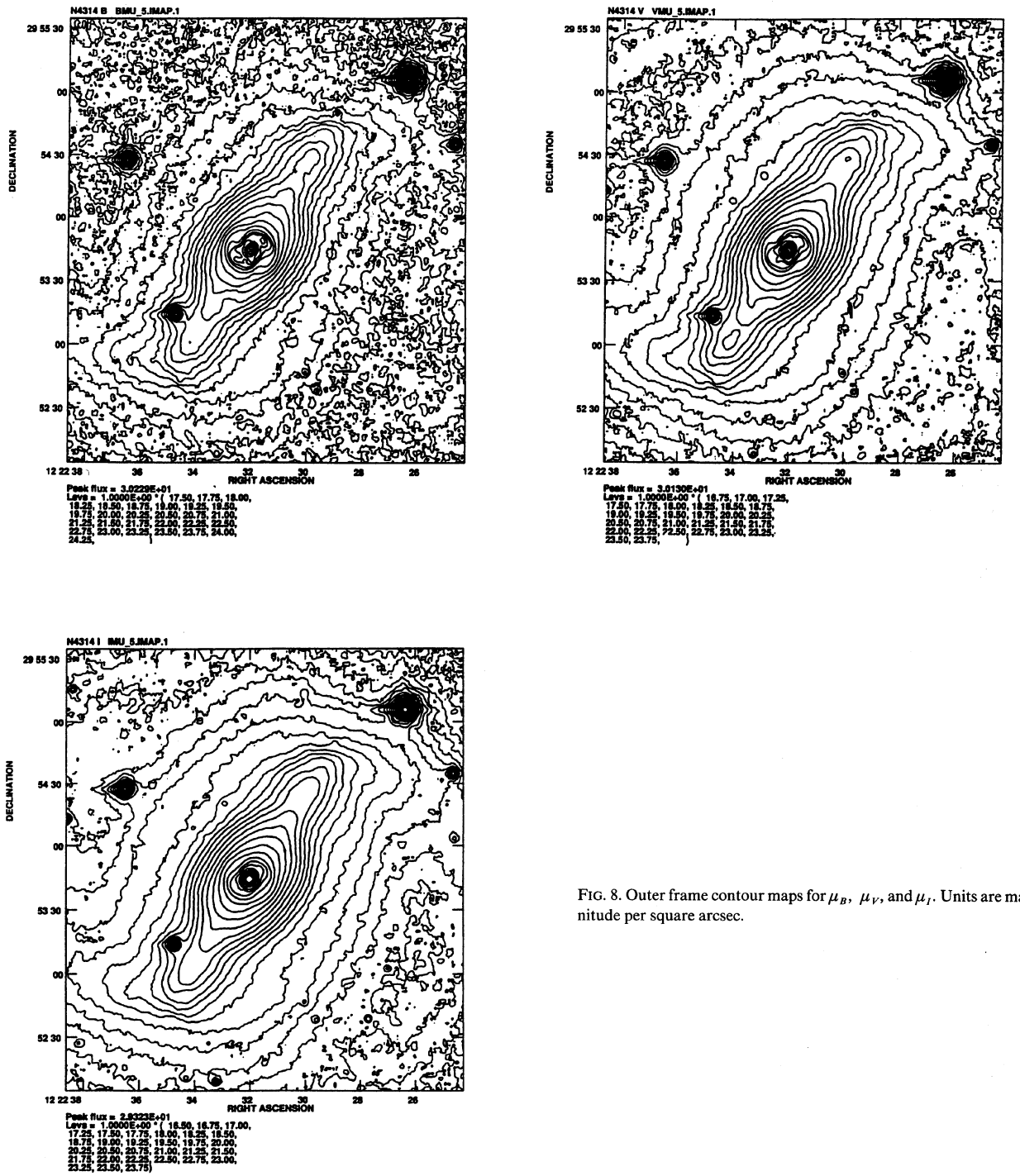

FIG. 8. Outer frame contour maps for μ_B, μ_V, and μ_I. Units are magnitude per square arcsec.

before and after NGC 4314; these show no elongation. The elongations are not caused by readout problems, improper stacking, or seeing (stars observed just before and after NGC 4314 have a round PSF). The elongation is not obvious in μ_B, μ_V, or μ_I.

To explore the faintest regions of NGC 4314 we scanned the E and O images on the Palomar Observatory–National Geographic Sky Survey (POSS) plates using the McDonald Observatory PDS microdensitometer. The aperture and step size were 5.03 arcsec. The scans covered a 1005×1005 arcsec region of the sky centered on the nucleus. The raw density data for the two images were registered and summed. We smoothed the resulting image with a 3×3 boxcar for a final resolution of 15.1 arcsec. The uncalibrated contour

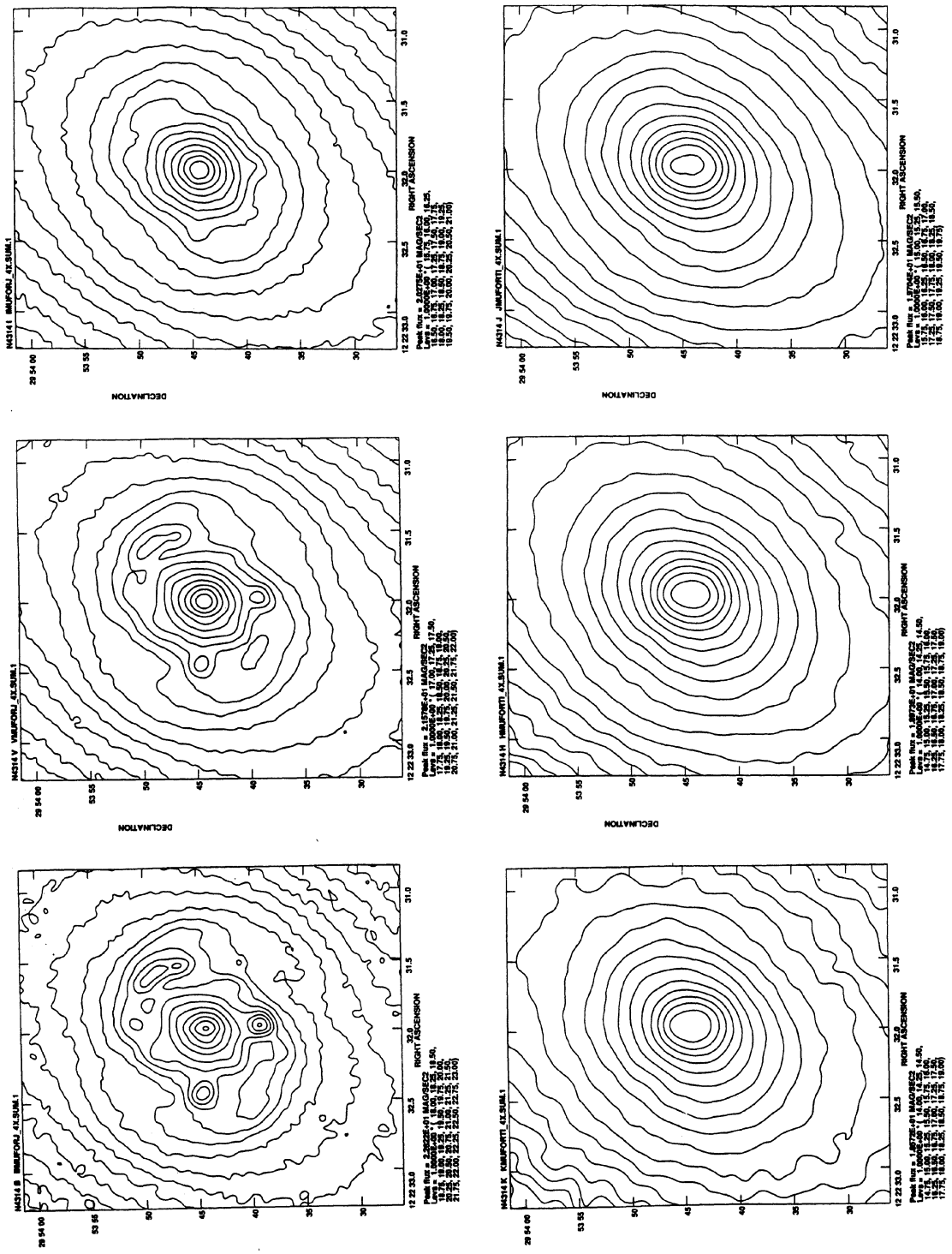

FIG. 9. Inner frame contour maps for (clockwise from upper left) μ_B, μ_V, μ_I, μ_J, μ_H, and μ_K. Units are magnitude per square arcsec.

map (Fig. 10) covers a 407×407 arcsec subset of the original scanned area.

Contour levels were chosen to highlight the bar, the spiral arms, and the lowest detectable levels in the galaxy. Compared with Fig. 8, we see that the calibrated CCD contour maps do not show the faintest detectable levels in the POSS data (indicated by the broken ring of islands). The faintest levels in the POSS data (represented by closed contours) are at $\mu_B \sim 24.3$, a brightness derived by comparison with the average profiles in Fig. 13 (see Sec. *5.3*). This level has an ellipticity $\epsilon = 0.08 \pm 0.02$ at a P.A. $= 59° \pm 8°$ ($r = 136$ arcsec), implying an inclination of $23° \pm 3°$. Grosbol (1985) obtained an inclination of 23° at a P.A. = 95° using only the red POSS plate. Note that virtually all the signal inside the outermost closed contour is affected either by the bar or by the spiral arms. Pure disk is accessible only at the faintest luminosity levels in the galaxy.

5.3 Luminosity and Color Profiles

Average surface magnitudes and colors versus radius were derived from synthetic aperture photometry. In Fig. 11 μ_B, μ_V, and μ_I surface magnitudes versus radius and μ_{B-V}, μ_{V-I}, and μ_{B-I} color indices versus radius are plotted for $r \leqslant 87$ arcsec. The radial limit was imposed by the TI CCD frame size and the placement of the galaxy within the frame.

We have extracted luminosity and color profiles parallel (P.A. = 148°) and perpendicular (P.A. = 58°) to the long axis of the bar. Figures 12(a) and 12(b) present average profiles for the inner 20 arcsec. For each average profile, the detailed profiles given in Fig. 14 are folded across the galaxy center and averaged. Each point in the detailed profiles is obtained by a four-point linear interpolation in the original

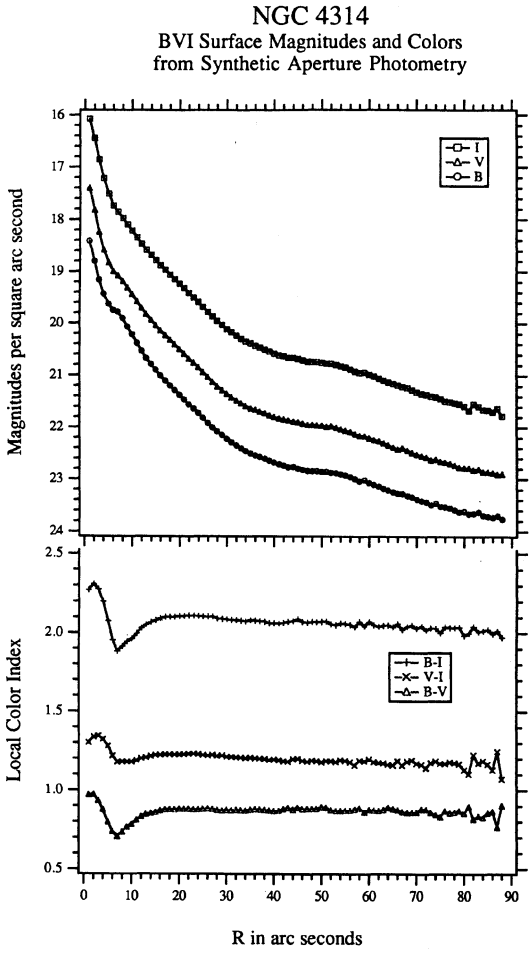

FIG. 11. Surface magnitude and color profiles obtained from synthetic aperture photometry. Note constancy of color except in the vicinity of the nuclear ring.

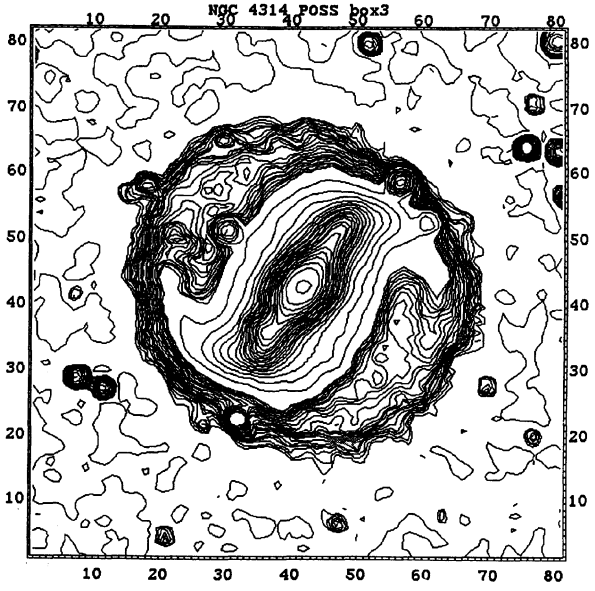

FIG. 10. Contour map of the sum of the POSS E and O plates scanned with a PDS microdensitometer. Frame size is 407×407 arcsec.

data array. Hence errors for the unsmoothed average profiles are $\sqrt{8}$ smaller than those given in Table 2. All the surface magnitudes are shown along with many color indices.

To extend the coverage of the average profiles to 100 arcsec along both axes for the *B*, *V*, and *I* data 2.5 [Figs. 13(a) and 13(b)], we have smoothed them to a 2.5 arcsec resolution. This shows trends better at faint surface-brightness levels. The smoothing results in typical errors of ± 0.06 mag at $\mu_B = 23$. In Fig. 13(b) we begin to sample the outer spiral arm for radii between 90 and 100 arcsec. The arms, within the errors, have the same colors as the bar and lens interior to these arms.

For numerical information concerning structure on the smallest spatial scales we turn to the detailed luminosity and color profiles exhibited in Figs. 14(a), 14(b), and 14(c). The position angles and paths of the detailed surface magnitude and color index profiles (P.A. = 148° and P.A. = 58°) are identified on a μ_{B-H} map of the inner 34×36 arcsec (Fig. 28). We also generated a profile passing through the bright H II region at P.A. = 90°, identified in WN as knot A.

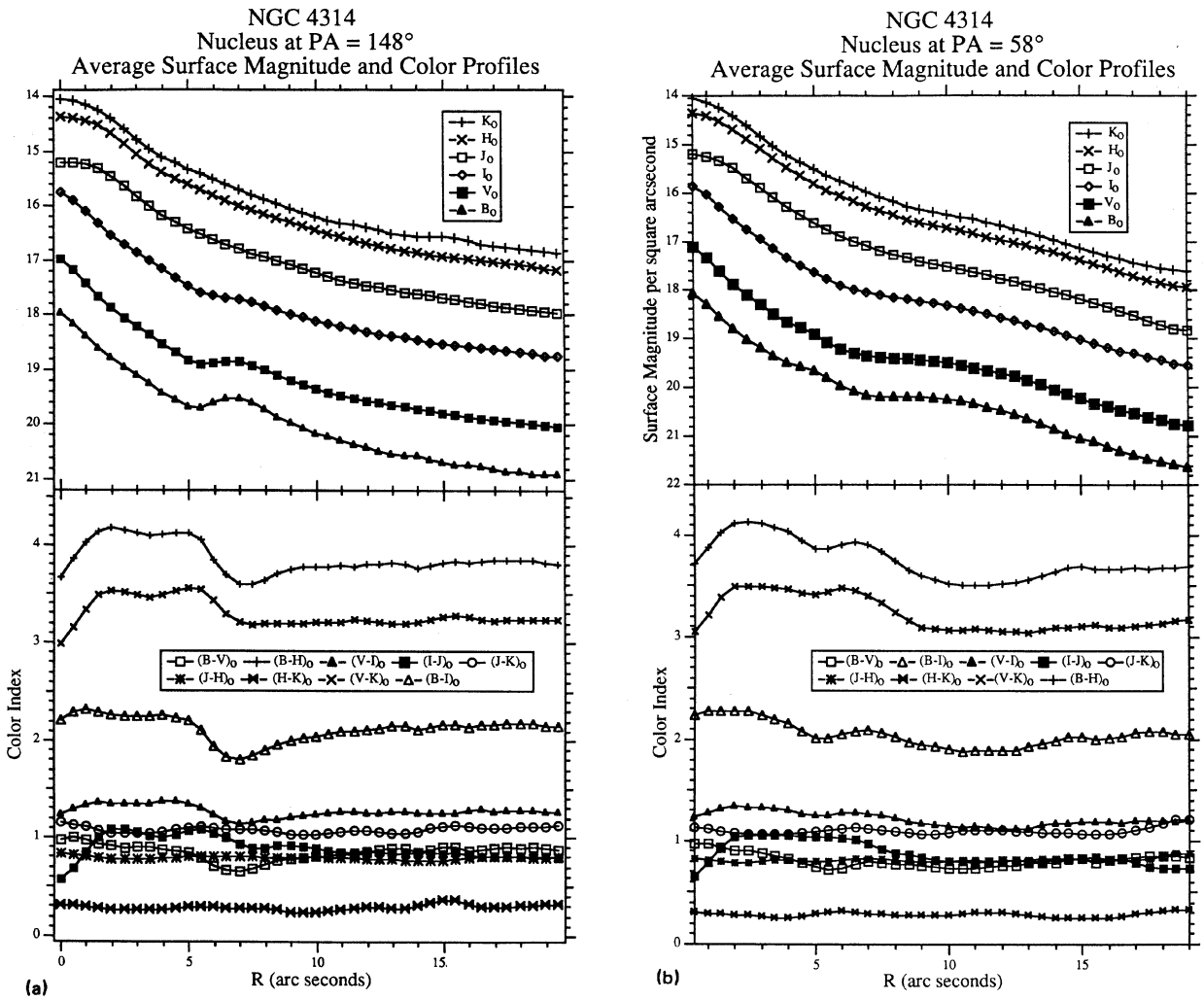

FIG. 12. Inner frame average surface magnitude and color profiles (a) along the bar at P.A. = 148°. (b) Same for axis perpendicular to long axis of the bar at P.A. = 58°. Values have been corrected for extinction due to our Galaxy. Internal errors are in most cases smaller than the symbol size (Table 2).

The profiles clearly show the effects of the changing point-spread function, with *B* as the best and the SWIR as the worst. The central blueing is almost certainly due to this effect. Note that at P.A. = 58°, the SW is redder than the NE. Along the bar, the reddening is similar on either side of the nucleus. This is expected behavior for the assumed orientation of this galaxy.

Finally, we can obtain *B*, *V*, and *I* surface magnitudes and associated color indices for the bar and lens of NGC 4314 from the outer frame detailed profiles. These profile positions and orientations are shown in Fig. 15. The detailed profiles are displayed in Figs. 16(a) and 16(b). The P.A. = 148° profiles have 1σ error bars attached on the NW side for the magnitudes and to the SE for the color indices.

5.4 Unsharp Masking

Since we are interested in comparing these results to future observations with the *Hubble Space Telescope* Wide Field Camera, we employed digital image processing techniques to our existing data to enhance as much of the small scale structure as possible.

One technique, unsharp masking, has long been used in the digital domain (Rosenfeld & Weszka 1976) to bring out high spatial frequency detail in 2D array data (e.g., Benedict 1982). For this application, no attempts have been made to preserve the photometric content of the resulting frames. They are useful only for enhancing smaller scale structure. For the full CCD frames, either a 17×17 pixel boxcar or a $1\sigma = 3$ arcsec (extending 4σ) kernel was used to produce the low-pass map. Subtracting the low-pass data from the original produces a high-pass map. To further increase S/N, we averaged together the *B*, *V*, and *I* images to make a new full CCD frame and then applied the masking technique. For the inner frames, which contain higher signal-to-noise data, we used a 5×5 pixel boxcar. To spare the reader from wading through multiple occurrences of "*J*-band high-pass map," we shall label resolution-enhanced maps by an "*hp*" subscript (e.g., BVI_{hp} for the averaged *B*, *V*, and *I* high-pass map).

One approach often used when dissecting a galaxy is to

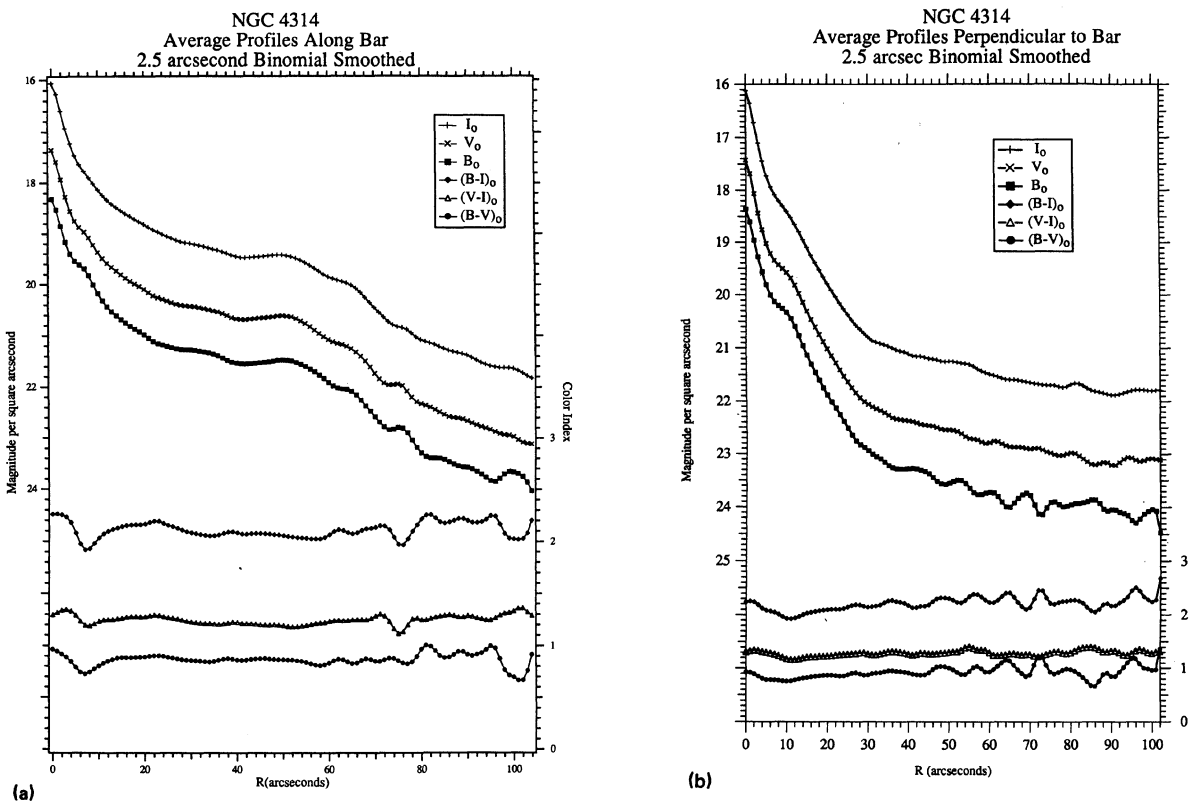

FIG. 13. Outer frame average surface magnitude and color profiles: (a) along the bar at P.A. = 148°. The blue region at $r = 72$ arcsec is object No. 5 in Table 1. (b) Same for the axis perpendicular to the bar at P.A. = 58°. The color variation at $r = 76$ arcsec is due to a CCD charge-transfer efficiency problem associated with object No. 2, Table 1. Profiles have been binomial smoothed to an equivalent resolution of 2.5 arcsec. Photometry has been corrected for extinction due to our Galaxy. Internal errors are in most cases smaller than the symbol size (reduce the values in Table 2 by a factor of 3.9).

first model the geometrically simple components (i.e., the bulge, disk, and bar) and then subtract these from the galaxy. By doing so, unmodeled components, such as spiral arms and rings, can be more easily studied. Unsharp masking is a "dime-store" version of this approach in the sense of reduced computing facilities and time.

Figure 17 [Plate 62] shows the results of unsharp masking the full outer frame for NGC 4314 (BVI_{hp}). Comparing with μ_{V-I} [Fig. 5(b)], we note that the enhancement process has increased the visibility of the outer dust lanes in the bar, especially to the northwest. The spiral nature of the material just outside the nuclear ring is easily seen. The nuclear spiral arms end abruptly just before they would have crossed the dust lanes in the bar. Their inner ends coincide with the ring. Possible dust arcs can be seen just exterior to the inner spiral at P.A. = 120° and 300°.

Note the multiple concentrations within the bar, which, with the exception of the "blobs" at the ends of the bar, were unexpected. We also detect shells of relative excess stellar material in the lens, especially strong to the N (R.A. = 12^h 22^m 34^s, Dec. = +29° 54′ 30″). The shells are similar, in shape and location, to the supposed inner arms seen in a low contrast print of NGC 5101 (Laustsen *et al.* 1987). They are also similar to the inner ring of NGC 1433 (Buta 1986). Finally, note a band of relative stellar deficiency outlining the bulge and bar.

The only structures in this map which are solely a result of the sharpening process are the halos around the foreground stars. These halos change size as we vary the smoothing used to produce the low-pass map. None of the other structures change shape, size, or location as the characteristics of the low-pass map are varied.

I_{hp} {Fig. 18(a) [Plate 63]} shows a pattern remarkably similar to that seen in μ_{V-I} (Fig. 7). J_{hp} [Fig. 18(c)] shows three major regions of locally lower signal. The darkest patches in J_{hp} coincide with "breaks" in the H II ring, seen for example in μ_{V-I} (Fig. 7) and in Pogge [1989; Fig. 9(c)]. The J_{hp} dark patches just NE and SW of the nucleus coincide with dust from μ_{I-J} [Fig. 7(b)]. A contrast enhanced version of J_{hp} [Fig. 18(c)] brings out darker arcs exterior to the spiral structure to the north and northwest (at R.A. = 12^h 22^m 31.5^s, Dec. = +29° 53′ 53″), and to the south and southeast (at R.A. = 12^h 22^m 32.5^s, Dec. = +29° 53′ 35″). These arise from less than 3% variations in intensity. We detect clumps of excess signal between the inner dust and these outer arcs (e.g., at R.A. = 12^h 22^m 31.5^s, Dec. = +29° 53′ 50″). These clumps are also visible on I_{hp} and on the contrast enhanced and greyscale-reversed I_{hp} [Fig. 18(b)], though they are much broader and a bit closer to the ring. Figure 18(b) clearly shows that the nuclear spiral arms do not "end" at the linear dust lanes. One sees a faint bridging of the lanes, especially for the southwest arm (at R.A. = 12^h 22^m 31.9^s,

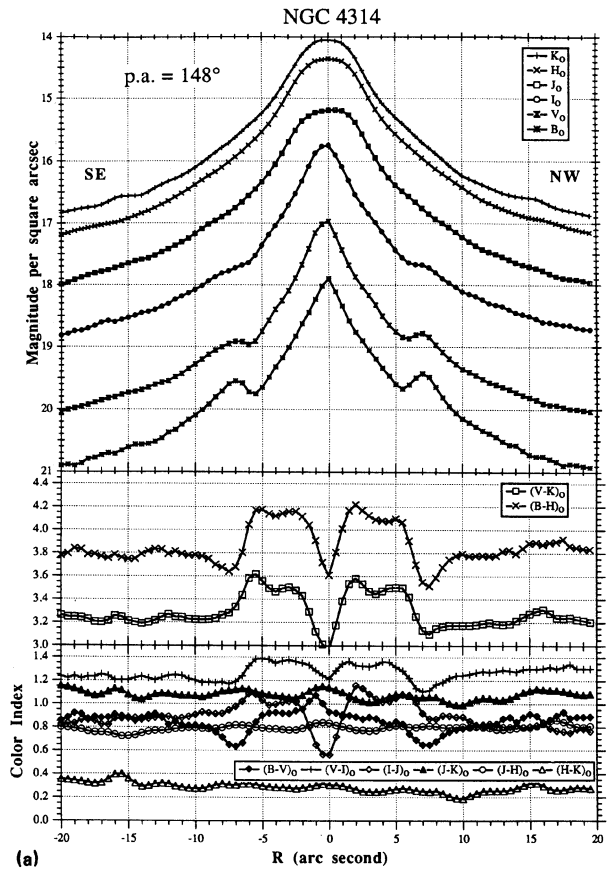

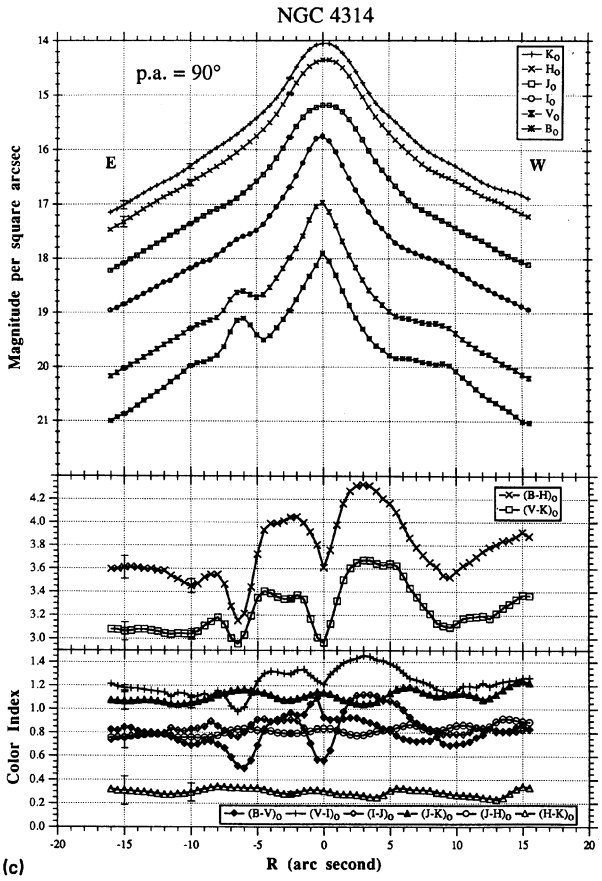

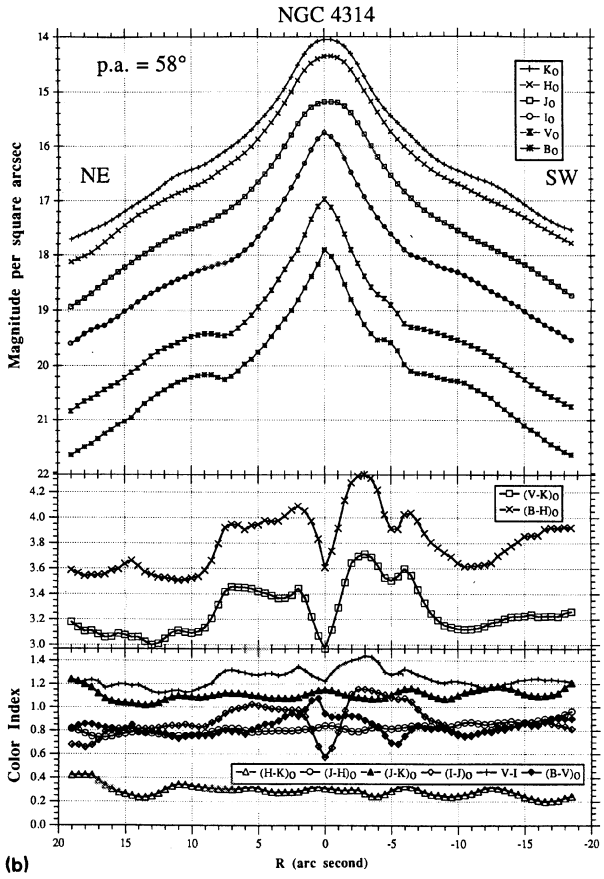

FIG. 14. Inner frame detailed surface brightness and color index profiles (a) along the bar, (b) perpendicular to the bar, and (c) through the H II region denoted knot A by WN. Values have been corrected for extinction due to our Galaxy. 1σ error bars are attached to several points to the east on the profiles in (c). The paths for (a) and (b) are identified in Fig. 28.

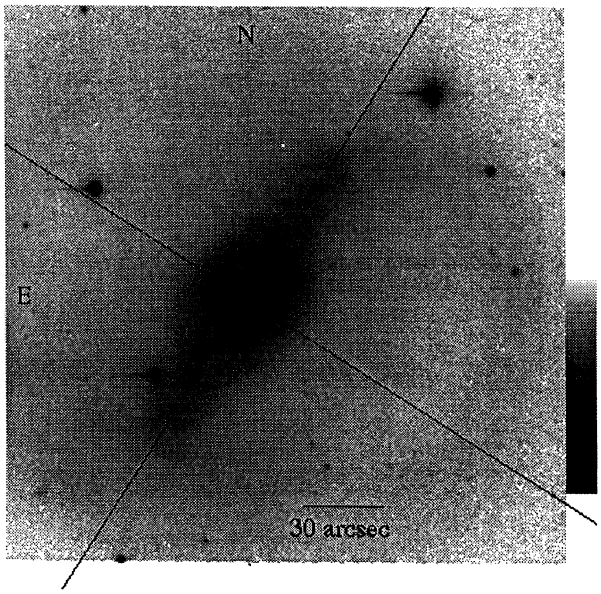

FIG. 15. The along bar (P.A. = 148°) and cross bar (P.A. = 58°) profile orientations are identified on a B greyscale map for the outer frame.

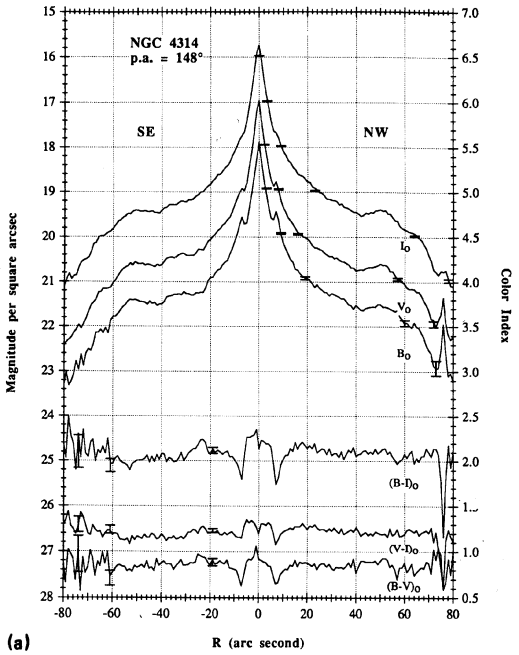

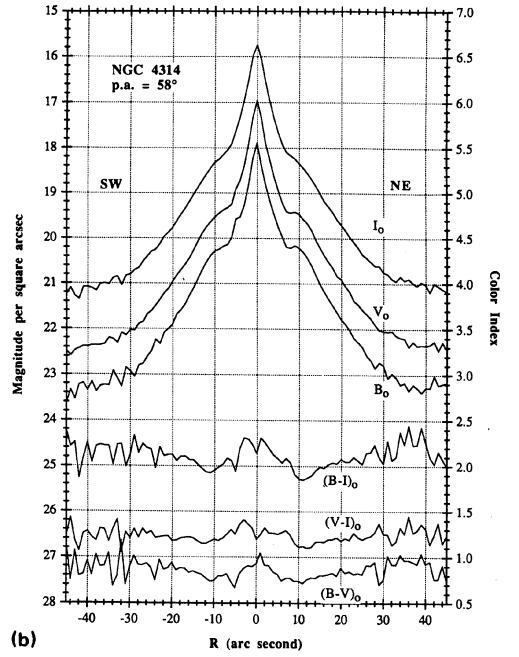

FIG. 16. Detailed B, V, and I surface magnitude and $B-V$, $V-I$, and $B-I$ color index profiles for the outer frame (a) along the bar at P.A. = 148° and (b) perpendicular to the bar at P.A. = 58°. Error bars for (a) are 1σ.

Dec. = +29° 53′ 34″). Lastly, the nuclear bar at P.A. = 136° begins to look suspiciously like an artifact produced by masking dust in Fig. 18(b).

6. INTERPRETING THE MAPS AND PROFILES

The maps and profiles raise many basic questions. From Fig. 18(c), what is the nature of the dust lanes in the bar and in the ring environment? Is there one color index (Fig. 7) which best traces the dust? Can NGC 4314 be decomposed into some minimum set of organizational components such as a bar, nucleus, lens, and disk? What is the symmetric structure (Fig. 17) in the bar? Are both nuclear bars (Figs. 6, 7, 9, 18) real? Why is star formation seemingly concentrated in the nuclear ring and why are there newer stars external to the nuclear ring? Is the nuclear spiral [Fig. 18(b)] a stellar feature? How is it generated and maintained? What is the source of the gas for the present day star formation? What are the spiral-shaped low-signal regions seen [Fig. 18(c)] in the SWIR enhanced maps?

The objects radiating and/or modifying the flux we and others have captured from 0.4 to 2×10^5 μm wavelength include stars, new and evolved. Dust in the galaxy includes hot dust, emitting radiation and cold dust, selectively scattering radiation. Gas in the galaxy can contribute line and free-free emission. To disentangle which sources contribute at which locations in NGC 4314, we first discuss various interpretations which can be applied to these data. With these interpretive aids we shall then explore the surface magnitude and color index maps to answer some, but not all, of the questioned posed above.

6.1 Interpretations

We start with a fairly obvious observation: unsharp masking emphasizes regions of rapid change of brightness, that is, regions where conditions are changing on short distance scales. Comparing I_{hp}, Fig. 18(a), with μ_{I-J} (Fig. 7) confirms that dust lanes are more easily seen in the unsharp masked frames. Comparing I_{hp} with μ_{B-H} (Fig. 7) suggests that regions of recent star formation are also more easily detected. The technique can find peaks as well as valleys. Excesses in signal detected without associated color changes can be interpreted as changes in stellar surface density, not changes in stellar population or dust concentration.

The color index μ_{I-J} shows the greatest contrast between dust and the surrounding stellar material. This is apparent from the surface color maps, Fig. 7, and in the profiles in Fig. 14. The index μ_{B-V} indicates the presence of dust (Benedict 1980, 1982), but not as well as μ_{I-J} and μ_{V-K} and, to a lesser extent, μ_{V-I}. The reason for this is the scattering of blue light by dust (Thronson *et al.* 1990). This effect is discussed in Sec. *7.3*. The index μ_{B-V} also traces new stars.

Tilanus *et al.* (1988) have shown for M51 that 6 cm radio emission is correlated with thermal emission from H II regions. They have also demonstrated a coincidence between 20 cm nonthermal emission and dust. Relativistic electrons from supernovae are another possible generator of 20 cm nonthermal emission (Lequeux 1990).

Vogel *et al.* (1988) have shown for M51, a galaxy with a very strong density wave, that CO(2-1) emission coincides with visible dust. However, this association of CO with dust lanes is not universally true, as shown by recent work on M83 (Kenney & Lord 1991), a galaxy with a weaker density wave. We must therefore exercise caution when invoking a dust-CO correlation for NGC 4314.

Vogel *et al.* (1988) have demonstrated (also for M51) that the offset between dust lanes and Hα is an offset between star-forming molecular gas accelerated by a density wave and newly formed OB stars. This is expected if stars form a short time after the clouds have been perturbed by a density wave. They posit a 30 Myr delay between the density wave trigger and the appearance of massive stars. For M51 the new stars lie downstream from the molecular clouds. These are the observed consequences of the standard model for spiral density wave-mediated star formation.

Hα measures the rate of formation of high-mass stars and, in the absence of dust, traces the present day star formation rate, since stars producing the Hα signal have lifetimes on the order of 3×10^6 yr (Vogel *et al.* 1988). Blue light measures star formation rate integrated over the last 2×10^9 yr.

μ_{B-H} traces the locations of new stars (Bothun & Gregg, 1990; Bothun *et al.* 1984). This is clearly corroborated by comparing our Fig. 7 with the Hα map of Pogge (1989) and the 6 cm map of GB II.

The SWIR data presumably trace the distribution of stars, rather than gas and dust. μ_{J-K} is fairly insensitive to contributions from new, blue stars (disputed, however, by Thronson *et al.* 1990) but can indicate the presence of AGB population (Persson *et al.* 1983, Bothun *et al.* 1984). μ_{J-K} will also increase in the presence of significant dust (Telesco *et al.* 1982). A rise in μ_{J-K} with no other indication of dust might suggest red supergiant stars.

μ_{H-K} is claimed to be much less sensitive to dust than μ_{J-H} (Carico *et al.* 1990; Hutchings *et al.* 1990). Thronson *et al.* (1990) suggest that μ_H best represents the distribution of red giants, supergiants, and low-mass dwarfs. μ_H traces stars only, while μ_K can be perturbed by hot dust and μ_J by hot, young stars. Campbell & Terlevich (1984) contend that up to 35% of the μ_J flux could be produced by H line emission (Paschen β and γ) in giant H II regions. Thus a reddening in μ_{H-K} near a H II region might be identified with hot dust, and a corresponding blueing in μ_{J-H} might be expected.

For convenience, we have collected the interpretations discussed above into Table 3.

6.2 Exploring the Maps and Profiles

Figures 4, 5, 6, 7, 17, and 18 provide a variety of bandpasses, color indices, and enhancements. What can we learn from them, applying the interpretive aids just presented? Do they answer any of the questions raised above? For many of the features discussed below, surface magnitudes, colors, and radial distances can be determined from Figs. 14 and 16, the detailed luminosity and color profiles.

We organize our discussion of these maps by structural component, from the inside to the outside. These components are: the nucleus and nuclear bars; the nuclear ring and associated H II regions; the area between the nuclear bar and the nuclear ring; the locus of newer stars just exterior to the nuclear ring (i.e., the nuclear spiral); and the bar.

Again, for convenience, Table 4 collects together the major results of our multibandpass intercomparisons.

6.2.1 Nucleus and nuclear bars

Radio emission at 6 cm is weak to nonexistent at the nucleus, so we cannot ascribe the nuclear reddening seen in

TABLE 3. NGC 4314, 0.4–200 000 μm. Interpreting the maps.

BVI_{hp}, I_{hp} and J_{hp}	Emphasize regions of rapid change of brightness. Equivalent to subtracting a featureless model from the original. Highlights dust lanes, dust clumps, clumps of stars, and H II regions.
I_{hp}, μ_{I-J}	Changes in high-pass maps without corresponding changes in color index maps indicate stellar surface density variations.
μ_{I-J}	Indicates the presence of dust.
6 cm	Correlated with thermal emission from dust heated by young stars in H II regions.
20 cm	Nonthermal emission from dust. Also, relativistic electrons produced by supernovae.
CO(2-1)	Coincides with dust for strong density wave galaxies.
Hα	Measures the rate of formation of high mass stars and traces the present day location of massive stars.
μ_{B-H}	Traces the locations of new stars.
μ_{J-K}	Increases in the presence of significant dust. May indicate the presence of AGB population.
μ_{H-K}	Claimed to be much less sensitive to dust than μ_{J-H}.
μ_H	Best represents the distribution of red giants, supergiants, and low-mass dwarfs. μ_H traces stars only. μ_K can be perturbed by hot dust and μ_J by hot, young stars and hydrogen line emission.

TABLE 4. NGC 4314. Results from intercomparing maps.

BVI_{hp}, μ_{B-H}	Trace newer stars.
μ_{B-H}, $H\alpha$, 6 cm	No large, highly obscured (by dust) H II regions between the nuclear ring and the galaxy center. No current star formation within the nuclear stellar spiral external to the nuclear ring. The H II complex at P.A. = 26°, the most intense in both Hα and 6 cm, is quite weak in μ_{B-H}.
μ_{B-H}, μ_{V-I}	Color gradient along the arms of the nuclear spiral. Newer stars nearest the nuclear ring.
BVI_{hp}, μ_{I-J}	Trace the dust near the nuclear ring much better than μ_{B-V}.
BVI_{hp}, μ_{I-J}	Indicate that the dust lanes in the bar do not stop at the nuclear ring. They pierce the nuclear ring and then form a dust ring just interior to the nuclear ring of star formation.
μ_{I-J}, μ_{V-I}	Linear dust lanes leaving the vicinity of the nuclear ring at P.A. = 60° and 240° seem to branch just outside the nuclear ring.
20 cm, Hα, 6 cm, BVI_{hp}	The ridgeline of 20 cm is between the most intense dust and present day star formation at the nuclear ring.
μ_{J-K}, BVI_{hp}	Most μ_{J-K} reddening due to dust. Some reddening, near H II regions, possibly due to AGB stars. Slight blueing at H II regions.
J_{hp}, BVI_{hp}	Trace the most optically thick dust. J_{hp} unaffected by H II regions, knots A and B.
J_{hp}, CO	Enhanced frame shows spiral gaps due to dust, outboard from the nuclear spiral.
μ_{I-J}	All reddening for this index is associated with dust.

μ_{J-K} to newly formed supergiant stars. It is either dust or, more likely, PSF mismatch.

The nuclear elongation, or bar at P.A. = 0°, seen in the μ_J, μ_H, and μ_K contour maps (Fig. 9), may be real. The feature, extending about 1.5 arcsec on either side of the nucleus, if real, is similar to that seen in other galaxies, for example, NGC 1291 (de Vaucouleurs 1975). The redder extension north and south of the nucleus in μ_{I-J} (Fig. 7) is not dust, but is due to this feature.

The other nuclear bar, prominent in μ_B [Figs. 6 and 18(b)], aligned along P.A. = 136° and nearly filling the nuclear ring, is at least partially due to dust, identified in μ_{I-J} [Fig. 7(b)], outlining a bar-shaped region.

6.2.2 The nuclear ring and associated H II regions

Next we discuss the nuclear ring, which is the most prominent feature in the inner frame. We detect the nuclear ring in all indices (Fig. 7). This ring is similar in spatial extent to that seen in the Hα map of Pogge (1989) and the 6 cm map of GB II.

Comparing μ_{J-K} and J_{hp}, we see μ_{J-K} become redder due to dust, especially at R.A. = 12^h 22^m 32.3^s, Dec. = +29° 53′ 50″ and R.A. = 12^h 22^m 31.5^s, Dec. = +29° 53′ 40″, near where the dust lanes cross the nuclear ring. Where μ_{J-K} is redder and J_{hp} is relatively flat (near the H II region, knot A) one could surmise the existence of hot dust or AGB stars. Other major regions of reddening are near the H II region at P.A. = 90° and a region on the ring at P.A. = 270°. The reddest sections in μ_{J-K}, lie virtually on top of the ring defined by Hα and 6 cm. To have an effect at these wavelengths requires much dust or relatively hot dust. This explains why the new stars are not particularly blue in the visible wavelength indices. The entire ring is riddled with dust. The H II regions and dust making up the ring are probably well mixed.

μ_{J-H} is similar to μ_{J-K}, with reddening near knots A and B, and slight blueing precisely at their locations, and is consistent with μ_J detecting new stars.

These new color index data allow us to determine some of the properties of the H II regions near and within the nuclear ring. Comparing our μ_{B-H} map (Fig. 7), the Hα map of Pogge (1989), and a 6 cm map (GB II, Fig. 7), there are evidently no large, highly obscured (by dust) H II regions between the ring and the galaxy center. This comparison does indicate a few heavily obscured sites of new star formation within the ring boundaries at R.A. = 12^h 22^m 32.25^s, Dec. = +29° 53′ 41″ and R.A. = 12^h 22^m 31.6^s, Dec. = +29° 53′ 41″. The H II complex at P.A. = 26° (R.A. = 12^h 22^m 32.2^s, Dec. = +29° 53′ 49″), the most intense in both Hα and 6 cm, is weak in μ_{B-H}. A 6 cm peak in the ring near knot B is not coincident with knot B, but lies a few arcsec east of the peak in μ_{B-H}. The morphology of the μ_{J-K} map suggests that there is more dust just to the east of knot B than at knot B. Much of the visible emission at this star formation site may be blocked by dust.

The hydrogen emission line component in the *J* bandpass is not particularly intense in the H II regions, as shown by the J_{hp} map [Fig. 18(d)]. We see no relative excess at the locations of the H II regions. The locations of knots A and B are dominated by relative deficits, most likely due to dust.

Other relatively red μ_{H-K} regions sit on top of the H II regions, knots A and B. These are likely to be hot dust. According to Telesco & Gatley (1984), μ_{J-H} should drop and μ_{H-K} rise at H II regions from associated dust and new stars. We see this in our data.

6.2.3 Between the nuclear bar and the nuclear ring

The region between the nucleus and the nuclear ring has some distinctive photometric properties. μ_{B-V} seems to indicate that the interior of the ring is uniformly awash in dust. However, μ_{I-J} [Fig. 7(b)] resolves this pool into specific lanes and I_{hp} [Fig. 18(a)] resolves the lanes into clumps, showing that the dust distribution inside the ring is far from uniform. Note the relative constancy of the μ_{B-V} profile and larger variations in the μ_{I-J} profiles (Figs. 14 and 16). We interpret these μ_{I-J} variations as indicating intense concentrations of dust. μ_{B-V} shows us all the dust, while μ_{I-J} shows only the greatest concentrations of dust. As a comparison between μ_{I-J} and μ_{V-I} shows, the dust lanes interior to the ring and located to the NW and SE are slightly further from the nucleus in μ_{I-J}. This separation is 1–2

arcsec [P.A. = 148° detailed profile, Fig. 14(a)]. Are we seeing an optical depth effect (the dust nearest the ring is deeper) or is there more (denser) dust nearer the ring? This might also be a scattering effect.

I_{hp} [Fig. 18(a)] and μ_{I-J} (Fig. 7) confirm that the dust lanes in the bar do not stop at the ring. They pierce the ring of new stars and H II regions and then form a ring just within the ring of star formation. Comparing I_{hp} with a 20 cm map (GB II, Fig. 7), we find some support for the assertion that 20 cm traces dust. However, the maximum 20 cm is not exactly coincident with the strong dust lanes. There is some tendency for the 20 cm to lie between the dust traced by I_{hp} and μ_{I-J} and the new stars traced by μ_{B-H} and 6 cm. On the other hand, 20 cm emission is strong at P.A. = 200°, where there is dust and weaker 6 cm emission. Also, the interior of the ring is more thoroughly filled in at 20 cm.

We see three regions of rapidly changing structure in J_{hp} [Fig. 18(c)]. Two of these are near the ring gaps and dust seen in I_{hp} and μ_{I-J} (see Sec. *5.4* for positions). The third, at R.A. = $12^h\ 22^m\ 31.8^s$, Dec. = + 29° 53′ 39″, coincides with a H II region that is moderately strong in 6 cm, but relatively weak in Hα. Comparing with μ_{I-J} (Fig. 7), we see that this last H II region also sits in dust.

We know that where μ_{I-J} indicates reddening, decreases in I_{hp} indicate dust. If μ_{J-K} and J_{hp} have a similar relationship, then dust would be responsible for any of the μ_{J-K} reddening in regions where J_{hp} decreases rapidly (except for the SWIR nuclear bar). Where μ_{J-K} is red and J_{hp} shows little dust, we could invoke hot dust or red supergiants. Note also that while much of the visible wavelength reddening is distributed in a spiral pattern, the μ_{J-K} reddening is not. In particular, note the lack of μ_{J-K} reddening near knots A and B, the two brightest H II regions. These are logical sites for both hot dust and AGB stars.

In μ_{I-J}, the reddest dust is at $r = 6$ arcsec at P.A. = 160° (R.A. = $12^h\ 22^m\ 32.2^s$, Dec. = + 29° 53′ 39″). Curiously, it is not intense in J_{hp}. For μ_{H-K}, the reddest nonnuclear material is distributed in a roughly ring-shaped region, with the reddest values coincident with the dust seen in I_{hp} and J_{hp}. The reddest μ_{H-K} values coincide with the dust patch seen in J_{hp} at P.A. = 55° (R.A. = $12^h\ 22^m\ 32.45^s$, Dec. = + 29° 53′ 49″). We again stress that these *JHK* color index variations are very small. Throughout the entire region covered by our data, the colors fall within the range for red supergiant stars discussed by Campbell & Terlevich (1984).

6.2.4 The nuclear spiral

We have discussed the nucleus, nuclear bars, and the nuclear ring. Just outside the nuclear ring is what appears to be a nuclear spiral, tangent to the ring at the spiral's inner sections. In all indices (Fig. 7), the colors of the spiral arms redden as the arms get further away from the nuclear ring. We know that dust obscures the stellar nurseries at the nuclear ring. Is this reddening evidence of an age progression or of a particular dust distribution exterior to the ring? The arms are traceably different in color compared to the nucleus and bar. Both arms have a uniform (in color) background.

The arms also broaden with distance from the ring. We note [Fig. 18(b)] that neither the broadening nor the intensity of the spiral arms varies smoothly. There are at least three discrete jumps in both broadening and intensity. The brightest, bluest, and thinnest arm sections lie closest to the nuclear ring to the northwest and south. The broadest, reddest, and faintest sections are northeast and southwest. The color variations and broadening are detectable in the detained inner luminosity and color profiles (Figs. 14 and 16). One can follow both arms around clockwise by inspecting the P. A. = 148°, 90°, and 58° profiles. These arms can also be seen in the color images of Wray (1988). There is no evidence in the arms for ongoing star formation in any color index in Fig. 7, in the Hα map of Pogge (1989), nor in any radio continuum observation (GB II). There is no evidence in μ_I or μ_{I-J} for significant dust associated with these arms. Hence we conclude that we detect an age variation, newest stars nearest the ring. The three groupings within each arm may then correspond to three episodes of star formation, the most recent occurring at the ring.

6.2.5 The bar

Finally, we discuss the outermost region of NGC 4314 for which we have high signal-to-noise ratio data; that is, the outer, or major bar. BVI_{hp} (Fig. 17) presents us with a bar containing multiple regions of increased surface density of stars, as well as dust lanes and pools. We defer discussion of these features to the next section (Dust) and Sec. *9.1.3*, bar kinematics.

Comparing the profiles in Figs. 13(a) and 13(b), we confirm that NGC 4314 belongs to the flat-barred class of galaxies as defined by Elmegreen & Elmegreen (1985) and Baumgart & Peterson (1986). The very shallow radial profile along the bar (as compared to perpendicular to the bar) is a prominent characteristic of this class.

Another interesting feature in the bar, just outside the ring (compare the μ_{I-J} and μ_{V-I} maps in Fig. 7), is that the linear dust lanes leaving the vicinity of the ring at P.A. = 60° and 240° seem to branch just outside the ring. One tributary becomes the roughly linear dust lane on the leading edge of the bar; the other seems for a short distance to follow the outer edge of the nuclear spiral. This effect is much more apparent to the northwest.

7. DUST: MORPHOLOGY AND PHOTOMETRY

We have just collected together qualitative impressions from the color index and high-pass maps. There may be hints in the dust patterns concerning the processes involved in distributing the dust. We will determine quantitative photometric parameters describing the dust. We begin by discussing the morphology of the dust lanes in the bar which are so clearly exposed in the unsharp masked frame of Fig. 17. We next derive absorption parameters for the "dust bowl" in the southeast part of the bar. Lastly, we quantitatively explore the dust interior to the nuclear ring.

7.1 Dust Lanes in the Bar

The dust lanes in the bar of this galaxy do not have a morphology consistent with the lanes described by the standard model for barred galaxies (Roberts *et al.* 1979). That model predicts linear lanes at the leading edges of the bar that eventually fall into the nucleus. We see, especially in μ_{V-I} (Fig. 5), meandering lanes on the leading edge. These lanes terminate long before they reach the end of the bar. One can trace a return of the dust to the vicinity of the nucleus on the trailing edge and midline of the bar. This behavior of a dust lane in a bar is not predicted by Roberts *et al.* However, if we assume that the dust traces the gas distribu-

tion in the bar, we may actually be seeing the gas circulation streamlines. Compare Roberts *et al.*'s Fig. 6 with our Fig. 5. The circulation would be out of the nuclear region on the trailing sides (east side of southeast bar, west side of northwest bar) and back into the nucleus on the opposite sides, within the straighter sections of the dust lanes. The spatial and velocity resolution of the velocity field data available to us (WN, GB I, and II) are too low to solidly support this hypothesis. However, we shall see (Sec. *9.1.3*) that these data qualitatively support at least part of this scenario.

7.2 The "Dust Bowl"

The overall qualitative visual impressions of the dust associated with the bar can be turned to quantitative photometric parameters for at least one section of this galaxy. The dust bowl in the bar to the southeast at $r = 23$ arcsec is clearly detected in the major axis detailed profiles [Fig. 16(a)], in the *BVI* color indices (Fig. 5), and in the high-pass map (Fig. 17). It is apparently associated with the dust lane in the leading edge of the southeast bar. It is the only region in our data sets to satisfy a majority of the criteria specified by Brosch *et al.* (1985) required to establish reddening parameters for dust in external galaxies. To do so requires a smooth light distribution in the vicinity of the dust and requires that dips in the light distribution are caused by dust and not galaxy structure. One must also assume that there is no forward scattering of light and that there is no emission within the dust lane. Unfortunately, we must restrict ourselves to the *B*, *V*, and *I* bands, since the *J*, *H*, and *K* data have extremely low S/N and serious flat-field problems in this area.

A 1.1-arcsec-wide slice through the dust bowl at P.A. = 58° samples the dust bowl and the assumed unaffected bar to the northeast. We determine A_B, A_V, and A_I by folding smoothed (equivalent resolution 2.5 arcsec) profiles across the center line of the bar and by assuming bar symmetry. Knapen *et al.* (1990) have used this technique for the dust lane in the Sombrero Galaxy, NGC 4594. One of the advantages of this method is that the results are unaffected by errors in corrections for the reddening effects of our galaxy.

The reflected across-the-bar profiles in Fig. 19 agree for distances from the dust bowl greater than 10 arcsec. This indicates that our symmetry requirement is met. Subtracting the dashed from the solid line gives the absorption. If we plot A_B against A_V and A_V against A_I, Fig. 20, we derive $A_B/A_V = 1.35 \pm 0.03$ and $A_I/A_V = 0.38 \pm 0.02$. In comparison $A_B/A_V = 1.2$ and $A_I/A_V = 0.52$ for NGC 4594 (Knapen *et al.* 1990). These absorption ratios imply $R = A_V/\mathrm{E}(B-V) = 2.86$ and $\mathrm{E}(I-V)/\mathrm{E}(B-V) = -1.77$, compared to $R = 3.1$ and $\mathrm{E}(I-V)/\mathrm{E}(B-V) = -1.6$ for our Galaxy (Savage & Mathis 1979).

The ratio A_I/A_V was derived from the entire dust bowl. Only the east side of the bowl was used to derive A_B/A_V. The west side of the bowl shows a rim of significant *B* absorption just at the edge of the strongest *V* absorption. This is clearly seen by comparing the μ_{V-I} and μ_{B-V} profiles in Fig. 19. Hence the loop in the $A_B - A_V$ plane in Fig. 20. Positional mismatch could cause this effect, but is ruled out by appeal to μ_{B-V} (Fig. 5), which shows well-registered star images over the entire field. Comparing Figs. 5(a) and 5(b), we see that the bowl shape is rounder in μ_{B-V} than in μ_{V-I}. Dickman (1988) discusses sedimentation, where heavier, larger grains collect at the centers of quiescent dust clouds. Grain size can affect the absorption ratios. We cannot invoke sedimentation to explain the variation of the A_B/A_V ratio as a function of position within the dust bowl, since the variation seen here is in μ_B only and is at the edge of the bowl, not the center. Also, quiescence is not an expected attribute of bar dust lanes. To unravel this anomaly requires higher S/N optical and SWIR data.

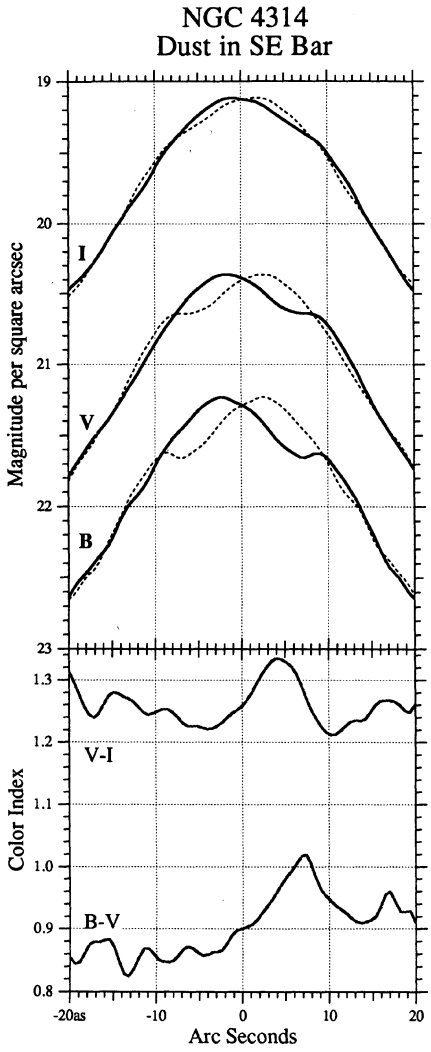

FIG. 19. *B*, *V*, and *I* surface brightness profiles perpendicular to the long axis of the bar through the "dust bowl." The solid line is the original profile, for which surface $B - V$ and $V - I$ are also presented. The dashed lines are the luminosity profiles flipped about the midpoint of the original profiles. The assumption of bar symmetry is supported by the agreement between the original and flipped profiles for $|r| > 10$ arcsec. Absorption values are derived by subtracting the original from the flipped profiles. Note the exponential distribution of stars away from the dust.

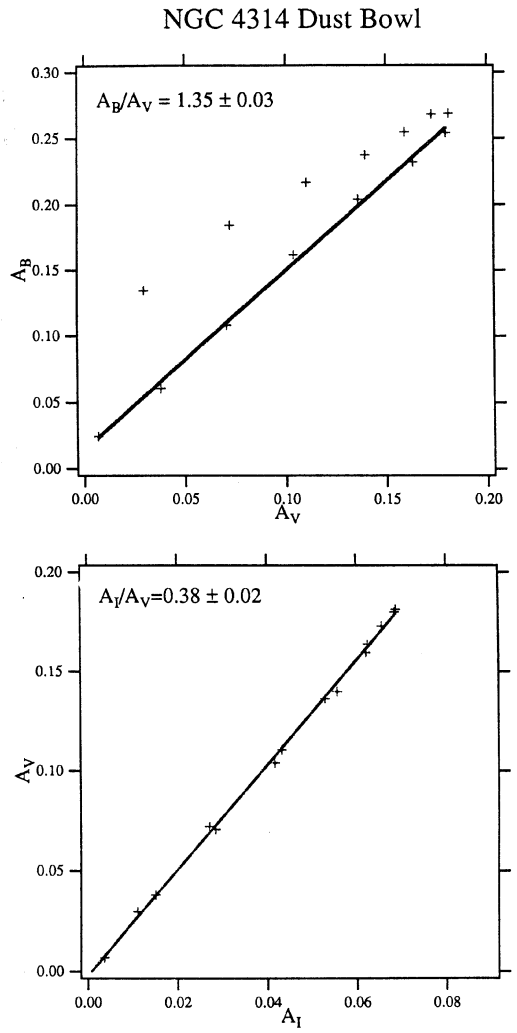

FIG. 20. A_B vs A_V and A_V vs A_I. Note the asymmetry in A_B vs A_V. This comes from the asymmetry in the $B-V$ color index profile seen in Fig. 19.

7.3 Dust Within and Interior to the Ring

We would like to derive similar information for the dust at and interior to the nuclear ring. We first draw attention to the "peculiar" reddening interior to the ring as shown by μ_{B-V} (Fig. 7). The reddening is extremely uniform. We see no large $E(B-V)$ values local to strong dust lanes within the ring. We cannot determine, as we did for the dust bowl, any extinction parameters for the dust lanes interior to the ring, since with no *a priori* knowledge of unobscured magnitude levels, estimations of A_B, A_V, and A_I are not possible. We can, however, make a somewhat less supportable assumption; that the unreddened stellar mix within, behind, and in front of the densest dust is similar to that found in the range $15 < r < 20$ arcsec along the major axis at P.A. = 148°. This area (indicated on Fig. 28 at $x = -9$, $y = -15$ arcsec) shows no signs of dust in any of the color index maps. We next assume that the gradients in μ_{B-V} and μ_{V-I} for the spheroidal and disk components are small over the 20 arcsec distance from the galaxy center to this location. We find support for this in Adamson *et al.* (1987) and Peletier *et al.* (1990). From the average profile of Fig. 12(a) we obtain for this region the assumed unreddened color indices listed in Table 5. These presumably unreddened colors are similar to the SWB IV-VI composite mix discussed in Persson *et al.* (1983) and Frogel (1985). Compared to the unreddened indices in Koornneef (1983), the mix contains late *M* to mid-*K* giants. According to Campbell & Terlevich, the unreddened colors are dominated by red supergiant stars (see their Fig. 1).

From the detailed inner frame profiles we measure the same indices for four dusty regions chosen from I_{hp} and μ_{I-J}. These are listed in Table 5. A quick inspection of the numbers indicates something odd. We see increased reddening in some, but not all of the indices. We then derive color excesses [$E(x-H)$, where x is *B*, *V*, *I*, *J*, *H*, and *K*] by comparing the dust lane colors with the presumably unreddened material. Figure 21 presents the color excesses for the four locations described in the caption. These are scaled to a Savage & Mathis (1979) reddening curve that is normalized to have $E(I-H) = 0.9$, and $A(\infty) = -0.6$. We derived A_V values from this standard Savage & Mathis (1979) red-

TABLE 5. Reddening and scattering in the vicinity of the nuclear ring.

Color index	Bar and nucleus unreddened	Dust lanes 148°	Dust lanes 238° $r=3$	Dust lanes 238° $r=6$	Dust lanes 270°	Unreddened H II region	Knot A
$V-K$	3.24	3.62	3.71	3.59	3.67	−0.55	2.96
$B-V$	0.89	0.84	0.89	0.75	0.90	−0.21	0.52
$I-J$	0.81	1.08	1.15	1.07	1.12	−0.19	0.82
$V-I$	1.27	1.38	1.44	1.33	1.46	−0.27	0.98
$H-K$	0.32	0.31	0.27	0.33	0.26	−0.03	0.33
$J-H$	0.79	0.80	0.81	0.82	0.78	−0.06	0.83
$J-K$	1.11	1.10	1.08	1.15	1.04	−0.09	1.16
$B-H$	3.81	4.15	4.33	4.01	4.31	−0.73	3.15
Color excesses $E(x-H)$, where x is							
B		0.33	0.52	0.20	0.40		3.88
V		0.36	0.52	0.34	0.43		3.15
I		0.27	0.35	0.27	0.26		1.90
J		0.01	0.02	0.00	−0.02		0.89
H		0.00	0.00	0.00	0.00		0.00
K		−0.01	0.05	−0.03	0.03		0.36

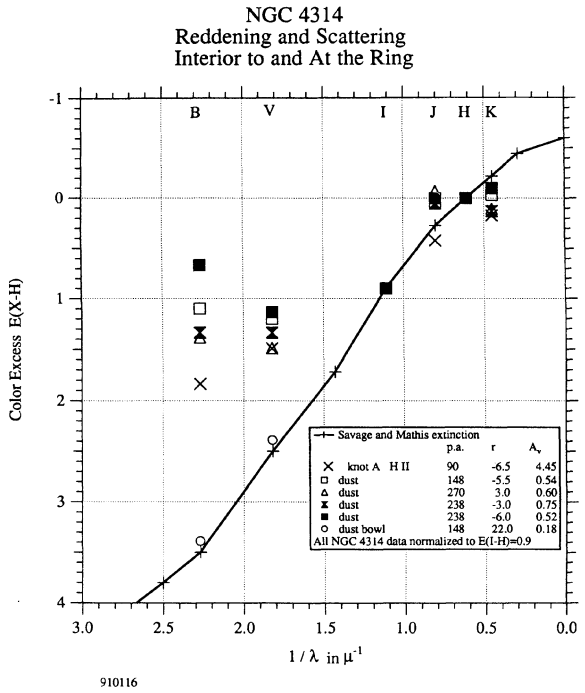

FIG. 21. Normalized extinction curves for dust at various locations within the nuclear region of NGC 4314. The solid line is a Savage & Mathis (1979) mean extinction curve normalized to produce $E(I-H)=0.9$. The infrared excesses agree with the mean curve much better than do the visible. We interpret the smaller visible excesses as scattering of the blue light produced by the stars newly formed in the nuclear ring. Note that the dust bowl, furthest from the nuclear ring, agrees best with the mean curve.

dening curve, then rescaled the A_V to reflect the actual measured excesses. These actual absorptions are the values presented in the legend.

The differences between the dust lanes interior to the ring of NGC 4314 and a standard reddening curve are significant (the formal errors in the color excesses are less than 0.03 mag), and are most likely due to scattered blue light at *B* and *V* (Thronson *et al.* 1990). The sampled dust regions are all close to sites of new star formation. Note that the sites showing the poorest agreement with the standard reddening curve in the *B* band are closest to the ring. With somewhat less certainty, one could ascribe the apparently decreased absorption at *J* to new stars within the dust lane and the apparently increased absorption in *K* to a stronger than normal signal from hot dust. It is now apparent why $I-J$ traces dust better than $B-V$, at least near the ring. The *B* and *V* bandpasses are much more affected by blue light from new stars in the ring being scattered from these dust lanes.

As a final probe into the conditions in the ring, we abstract [from the detailed profiles in Fig. 14(c)] color indices from the center of knot *A*, the H II region directly east of the nucleus. To produce color excesses, we assume $(B-V)_0$, $(V-I)_0$, and $(V-K)_0$ for a stellar and gas mix similar to that for the Orion Nebula (Tarrab 1982). We assume $(J-K)_0$, $(H-K)_0$, and $(J-H)_0$ for a supergiant B1 star from Koornneef (1983), since the $(V-K)_0$ for a B1 star matches the Tarrab $(V-K)_0$ for Orion. The unreddened and measured values are given in Table 5. We calculate an A_V value for the H II region in the same manner as above. The normalized reddening curve matches that of the dust lanes interior to the ring, although there is some indication that scattering in the *B* band is somewhat less in the H II region. The local extinction in knot A, $A_V=4.45$, is considerably more than the average extinction for six positions on the ring found by GB II ($A_V=2.7$) by comparing their 20 cm data with the Hα fluxes of WN.

Lastly, we scale and plot in Fig. 21 the color excesses for the peak reddening (in $V-I$) for the dust bowl profile of Fig. 19 and note the good agreement with the standard reddening curve. As one might expect, scattered light is much less an effect 800 pc from young stars.

Summarizing our exploration of the dust, the shapes of the lanes within the bars are suggestive of the gas streamlines discussed in several standard models for bar gas dynamics (Roberts *et al.* 1979). We have found Galaxy-like reddening characteristics in the dust bowl, a region far from the sites of new star formation. Near the sites of active star formation comprising the nuclear ring, we find evidence of scattering.

8. MODELING THE PHOTOMETRIC COMPONENTS

In this section we shall derive quantitative descriptions of several of the structural components of NGC 4314. In some cases this knowledge will assist us in making choices between competing theories concerning the mechanisms controlling the formation and subsequent distribution of stars within the galaxy.

8.1 The Old Stellar Distribution

We begin with the presumably oldest component, the old stellar distribution of the nucleus. The SWIR data are ideally suited to peer through the (in a sense) superficial features of new star formation near the nucleus. Ellipticity and P. A. as a function of *a*, the major axis radius, are plotted in Fig. 22 for the *I*, *J*, *H*, and *K* data. These were generated by fitting ellipses, spaced by 0.25 mag. Since the *I* band is obviously affected by the nuclear ring (see Figs. 6 and 9), we made no attempts to fit the *I* data at and near the ring, hence the gaps in the plots for *I*. Typical errors in *a*, the derived major axes, were less than 0.01 arcsec, while those for position angle averaged around 0.06°. The derived centers of the fitted ellipses had errors less than 0.01 arcsec, with positions that varied by at most 0.3 arcsec over the entire magnitude range. The trend in position angle with radius is similar for the four bandpasses, except in the center of the galaxy. A twisting of the isophotes is evident in each color, though not as pronounced in *I*.

The nuclear elongation in *J*, *H*, and *K* seen in the contour maps (Fig. 9) is evident in both ellipticity and P. A. with the three SWIR frames agreeing closely. However, the *I* band shows no hint of nuclear elongation. Once outside the nuclear ring/spiral the four colors track remarkably well, with the P.A. rising toward the outer bar value of 148°.

8.2 The Bar

It is possible to model the surface characteristics of the bar. Athanassoula *et al.* (1990) discuss one approach to modeling the shape of the bar, whereby the standard equation for an ellipse ($c=2$)

$$(x/a)^c+(y/b)^c=1$$

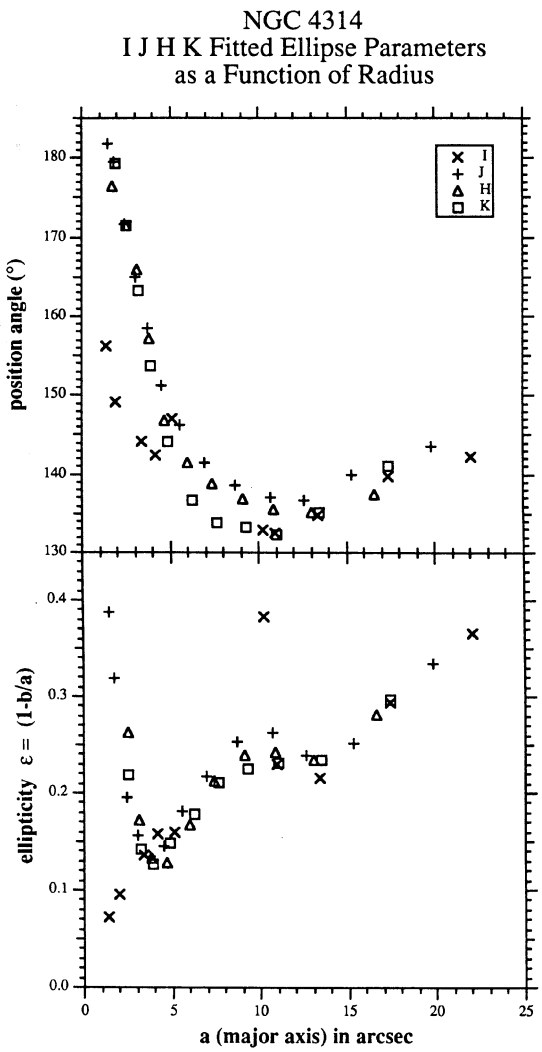

FIG. 22. Position angle and ellipticity as a function of major axis for ellipses fitted to the inner frame *I*, *J*, *H*, and *K* surface magnitudes. The nuclear bar is obvious in P.A. and ellipticity. All the band passes track one another, except for the nuclear bar ($a < 3$ arcsec) and a single point in *I* perturbed by the nuclear ring/spiral.

is generalized to produce more "boxy" than elliptical shapes for $c > 2$. The $\mu_I = 21.5$ contour in Fig. 23 is well represented by $a/b = 3$ and $c = 2.5$. It is difficult comparing this representation with the results of Athanassoula *et al.* since their results are given in units of bar length, a unit, as they point out, difficult to define for this galaxy (see our Sec. *9.1.3*). The contour maps in Fig. 8 illuminate the nature of this problem. Athanassoula *et al.* (1990) do obtain similar values for these bar parameters at 1.1 bar length. The value $\mu_I = 21.5$ [the brightness level for which our shape agrees with Athanassoula *et al.* (1990)] occurs at $r = 72$ arcsec on the average luminosity profile of Fig. 13(a), implying a bar length of 66 arcsec.

We have noted that NGC 4314 has a flat bar (a declining radial profile shallower than that of the disk alone, Elmegreen & Elmegreen 1985). What about the distribution of stars perpendicular to the bar in the plane of the galaxy? We

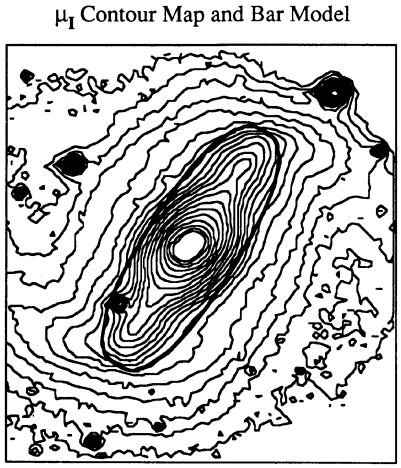

FIG. 23. μ_I contour map and Athanassoula *et al.* (1990) bar model fit to $\mu_I = 21.5$. The bar is represented by $(x/a)^c + (y/b)^c = 1$, where $a/b = 3$ and $c = 2.5$.

have one probe of this structure in the profile through the dust bowl (Fig. 19). Away from the bowl, the μ_B, μ_V, and μ_I profiles vary linearly with distance from the bar midline. Hence, the stellar density gradient across the bar is exponential. For the cross-bar range $10 < r < 20$ arcsec the average gradients are presented in Table 6. The μ_B and μ_V slopes are identical. The μ_I slope is slightly shallower.

8.3 Nuclear Spiral or Ellipse?

Let us turn our attention once more to the newer stars just exterior to the nuclear ring. We have been calling this the nuclear spiral. It really a spiral? Assuming that μ_{B-H} (Fig. 7) traces the location of newer stars, we would like to model this distribution. The shape of this distribution may offer some clue as to how these newer stars came to their present locations. A spiral distribution would suggest that star formation occurred at these sites at some time in the past. An elliptical distribution would support a process whereby these stars, once formed in the ring, move in orbits which take them away from the ring.

We first fit a spiral

$$r = r_0 e^{\theta\phi}$$

to this distribution. The best fit has $r_0 = 30.47 \pm 2.31$ arcsec and pitch angle $\theta = -12.7° \pm 0.9°$ with $\chi^2 = 4.22$.

As we shall see in Sec. *9.3*, it is possible that these newer stars belong to one of the orbit families associated with stel-

TABLE 6. Cross-bar average surface magnitude gradients for NGC 4314.

Bandpass	Gradient (mag kpc^{-1})
μ_B	2.00 ± 0.02
μ_V	1.99 ± 0.02
μ_I	1.92 ± 0.01

lar bars. If so, one might expect an elliptical distribution. Fitting to the same data points we obtain an ellipse with $a = 11.9 \pm 0.1$ arcsec, $b = 8.5 \pm 0.1$ arcsec, and P.A. $= 48.4° \pm 0.8°$ with $\chi^2 = 5.85$.

The original data points and fitted distributions are presented in Fig. 24. As can be seen, this test is inconclusive. Formally, the spiral is slightly favored.

8.4 The Nuclear Bulge

The nuclear bulges of many galaxies are found to follow the de Vaucouleurs $r^{1/4}$ law in the visible (Schombert & Bothun 1987) and in the SWIR (Adamson *et al.* 1987). Significant variation in the color index maps presented in Fig. 7 and in the detailed profiles of Fig. 14 argue strongly against even attempting to model the nucleus. As Fig. 21 illustrates, dust absorption in the *V*-band ranges from 0.5 to above 4 mag at the radius of the nuclear ring and interior to this ring. All the color indices show variations within the radial extent usually found to obey the de Vaucouleurs $r^{1/4}$ law.

With these caveats in mind, the *IJHK* profiles are plotted against $r^{1/4}$ in Fig. 25. Rather surprisingly, we find quite clean $r^{1/4}$ relationships, in spite of the presence of variable and strong absorption. We fit the profiles in the range $1.2 < r^{1/4} < 1.6$ ($2.07 < r < 6.55$ arcsec) with straight lines. The slopes and intercepts were then transformed into the effective radii and magnitudes (Capaccioli 1989) given in the key of Fig. 25. The slopes for all the colors are similar. A spheroidal distribution in the absence of the nuclear spiral would have small color gradients (e.g., Peletier *et al.* 1990; Boroson & Thompson 1987 for normal elliptical galaxies, and Adamson *et al.* 1987 for M83). The trend of effective radii, smaller for *J* and largest for *K*, is also seen for M83. These parameters are doubtless perturbed by the dust lanes known to exist within the fitting range. This will be particularly true for the *I*-band.

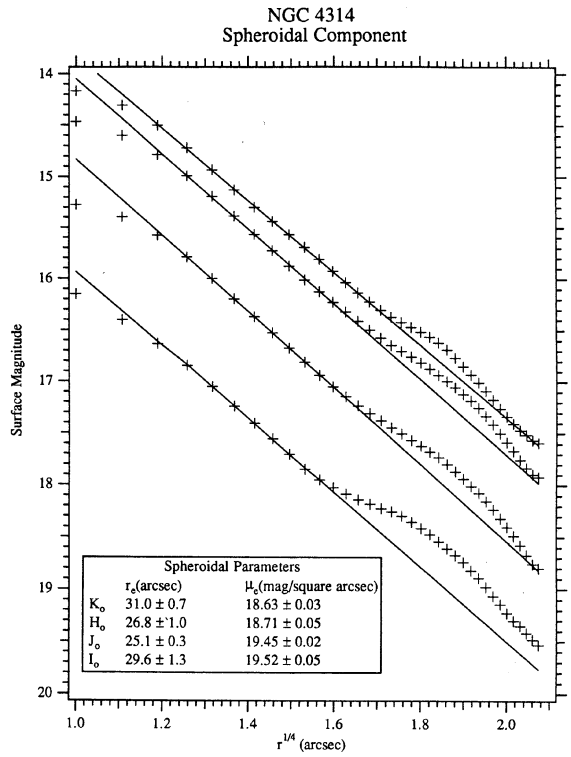

FIG. 25. Near-infrared (*I*) and short-wavelength infrared (*JHK*) surface magnitude profiles at P.A. = 58° plotted vs $r^{1/4}$. The *K* profile is at the top, the *I* at the bottom. The solid lines are the straight line fits to the surface magnitude values in the range $1.2 < r^{1/4} < 1.7$. Note the similarities in slope (e.g., effective radii) and the excess over the $r^{1/4}$ distribution at $r^{1/4} = 1.8 = 10.5$ arcsec in all bandpasses.

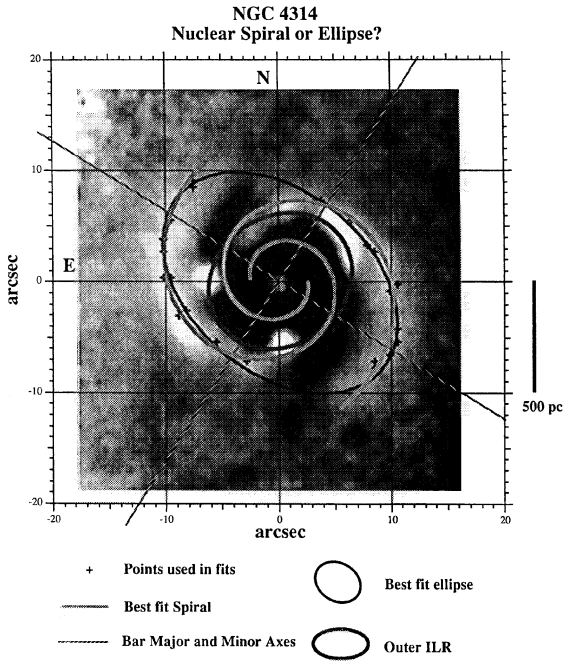

FIG. 24. A contrast enhanced μ_{B-H} map with the spiral and ellipse best fits from Sec. *8.3*. The points used in the solutions are marked +. Comparing χ^2, the spiral is favored slightly over the ellipse. However, note that the major axis of the ellipse is very nearly perpendicular to the bar major axis, as required by the x_4 family.

The principal results of this effort are not the photometric parameters of the nuclear bulge. Rather, note the excess intensities over the spheroidal component, peaking near $r^{1/4} = 1.8$, or $r = 11$ arcsec *in all SWIR bandpasses*. This excess corresponds to the nuclear spiral. This is a detection of a stellar component over and above the spheroidal distribution, a component exactly coincident with the nuclear spiral.

Typically, one models the spheroid (or bulge) and disk iteratively (e.g., Schombert & Bothun 1987), since the disk may make a small but finite contribution in the nuclear region, and similarly, the bulge perturbs the light levels usually attributed to the disk. From the faint levels shown in the P.A. = 58° average profiles [Fig. 13(b)], we can see that the disk of NGC 4314 is not a major structural component. Hence we incur little penalty in neglecting the disk.

Summarizing, our modeling has resulted in numerical descriptions of the distribution of the oldest stellar component

in NGC 4314, with the *I* band agreeing with the SWIR. Our derived bar shape is qualitatively similar to that obtained by Athanassoula *et al.* (1990). The bar [which is flat, as seen in the radial profiles in Figs. 13(a) and 16(a)] is shown to have an exponential cross section. The distribution of newer stars just outside the nuclear ring marginally favors a spiral. Finally, the SWIR allows us to cut through the near-nucleus dust and confirm an $r^{1/4}$ distribution for the nuclear bulge, with an excess signal in all bandpasses in the vicinity of the nuclear spiral.

9. STAR FORMATION

We now turn to a discussion of star formation in NGC 4314. There are sites of recent massive star formation in the nuclear ring. There is evidence of recent star formation and age variations in the nuclear spiral. Raw material, as indicated by dust, is present in the bar and at the nuclear ring. Are these related? Photometry provides a snapshot of the present distribution of stars and dust. Knowledge of the dynamics of these components can provide clues as to past and future location. Photometry and kinematics together may give us insight into the processes which have built and maintained the morphology of the nuclear region of NGC 4314 and of the major bar.

9.1 Kinematics

We have no new velocity field information to present in this paper. However, results from past investigations may provide us with information sufficient to begin to understand this galaxy. We shall first explore the coarse dynamics of the dust lanes, then examine photometric evidence for resonances within the bar.

The GB I and II data contain much more velocity information than discussed in GB II. Their measured positions and intensities are indicated on a μ_{B-H} map (Fig. 26) by circles denoting the 12.5 arcsec beam size of the GB I observations. We have examined the CO(2-1) spectral data presented in GB I (their Fig. 3) and note that in six of the eleven measurements, the spectra have twin peaks. The positions with double peaks are 2, 4, 5, 6, 7, and 8. The double peaks are signals from parcels of gas with differing radial velocities. A complete analysis of these spectra will be included in Paper III, when we present our new CO interferometer data. For now we discuss possible interpretations of the multiple peaks in the GB I data.

9.1.1 The nuclear ring

We assume for now, as in GB II (see also Combes & Gerin 1985) that the nuclear ring is the inner Lindblad resonance (ILR). WN present a Hα radial velocity curve for the inner 10 arcsec and estimate an inclination of $i = 30°$. They assume solid-body rotation for $r \leqslant 10$ arcsec and determine a dynamical line of nodes at P.A. = 121°. GB II have concluded that the same rotation found for Hα holds for CO. This result comes from convolving a 12.5 arcsec beam with a 12-arcsec-diam CO ring having a deprojected rotational velocity of 186 km s^{-1} and $i = 30°$, the WN values. They then compare this with a single CO spectrum and claim agreement (GB II Fig. 5).

The double-peaked spectrum for point 5, at the center, is probably due to the 12.5 arcsec beam size collecting signal from both sides of the rotation curve, although the average velocity of the two components relative to the observed systemic velocity ($V = 978$ km s^{-1}) is not zero. This may indicate that the chosen center of the CO distribution might not be the dynamical center of the galaxy. Alternatively, the nonzero average may reflect streaming motions near the nucleus such as those seen in NGC 6221 by Pence & Blackman (1984).

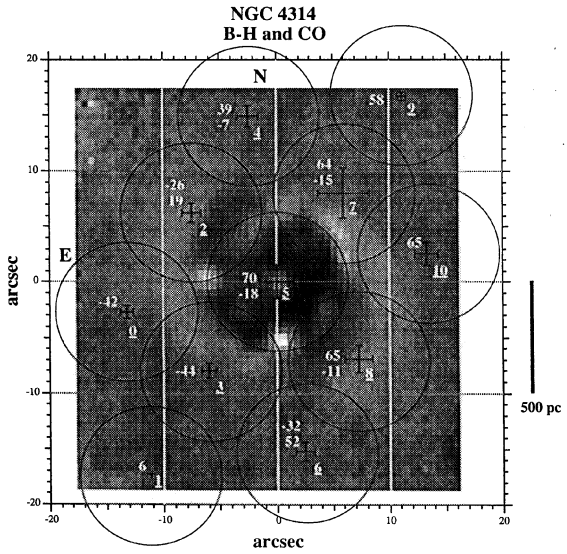

FIG. 26. The locations of the CO(2-1) measurements of GB I are plotted on a μ_{B-H} map. The circles represent the 12.5 arcsec beam. The cross size is proportional to the measured intensity of the strongest signal peak within each beam. The underlined number to the right of each circle center is the identification number referred to in the text. To the left of each beam center are the radial velocities referenced to a systemic velocity of 978 km s^{-1}. For those GB I spectra with twin peaks, we show two velocities, the velocity for the stronger peak on top. The correlation of multiple peaks with the bar-driven dust lanes is evident.

9.1.2 The dust lanes in the bar

From Fig. 26 we can see that the interior of the ring has a strong CO signature, consistent with the μ_{B-V} and μ_{I-J} dust signatures. The spatial resolution of the GB I and II data is high enough to detect CO exterior to the H II ring. In particular, the beam for locations 4, 6, and 9 cannot contain material from a ring with radius 6 arcsec. Hence, the dust lanes exterior to the ring, visible on I_{hp} and J_{hp} (Fig. 18), are detected in CO.

The bar dust lanes may be responsible for many of the secondary peaks seen in the GB I CO spectra. For example, one component of point 2 probably comes from CO associated with the ring. The other component may indicate noncircular motions associated with the nearby dust lane. This spectrum may be detecting material moving into the nuclear region along the dust lane, as predicted by various models (e.g., Roberts *et al.* 1979). This would explain the velocity of a component of point 4, which also lies on that dust lane. Similarly, point 6, near the SW dust lane, has a component reflecting the general rotation at that distance from the center, and a component with a larger radial velocity, indicating infall away from us, into the nucleus along the dust lane. That point 8 has two components also supports this assertion.

Point 7, the point that lies along the mid-line of the bar and just outside the NW section of the ring, sits directly on top of the flux deficit detected in the I_{hp} and J_{hp} maps (Fig. 18). One peak is most likely material associated with the CO ring postulated by GB II. The edge of the beam for point 7 catches a little of the NE dust lane (on the leading edge of the bar) discussed above in conjunction with point 4. We are unable to distinguish whether the two velocity components are associated with the CO ring and the weak dust signature seen in J_{hp} [Fig. 18(c)] or are associated with the dust seen best in the full-field μ_{V-I} map in Fig. 5. If, as discussed in Sec. *7.1* above, the shape of the dust lane reflects a gas circulation streamline (see also Tubbs 1982), the gas should be leaving the nucleus on this side, resulting in a secondary peak with a larger radial velocity relative to circular motion. We hope to resolve this uncertainty in Paper III. Point 3, which lies on the similar lane to the SE, shows only a single component.

In summary, many of the multiple peaks in the GB I and II CO data probably indicate noncircular streaming motions associated with the bar dust lanes.

9.1.3 Radially symmetric structure in the bar

Often the bar is treated as a density wave rotating within an otherwise axisymmetric disk (Bosma 1990). Quoting Bosma: "A lot of structure can occur in such a configuration, and resonances can be set up naturally." There is considerable structure in the bar which is not readily identifiable with dust using the color index maps. As shown in Fig. 17, the average BVI_{hp}, we see this structure within the bar on both sides of the center, for example at R.A. = $12^h22^m29.8^s$, Dec. = $+29°54'29''$ and R.A. = $12^h22^m34.3^s$, Dec. = $+29°53'00''$. The apparent visual symmetry of the clumps within the bar prompted us to produce Fig. 27. We have plotted the NW and SE profiles from the high-pass map on top of the major-axis average magnitude and color profiles. This vividly confirms the impression of radial symmetry of the bar structure, especially at 7 (nuclear ring), 22 (dust bowl), 36,52 (bar blobs), and 66 (end of bar) arcsec from the center. The minima are somewhat more symmetric than the maxima. The maxima and minima show little color differences when compared to the rest of the bar. The symmetry and uniform color of the peaks would argue that we are seeing a buildup of stars, rather than any masking effects from dust.

These regions of increased stellar surface density on each side of the bar may be from the looping behavior of stars following the x_1 orbits described by Teuben & Sanders (1985). Comparing their Fig. 2 with our Fig. 17 and scaling to a bar length of 6 kpc, one might identify the cross-over points with the enhanced stellar densities. The regions at the cross-over points will include stars on the way out to the bar end and stars moving back into the galaxy center.

Finally, why the dust lanes terminate long before reaching the bar ends remains a puzzle. This behavior suggests that corotation (CR) occurs closer in than the bar end. Combes (1988) points out that dust lanes either terminate or change direction at CR. Figure 17 shows the lanes of NGC 4314 ending at $r = 22$ arcsec; this fact supports the interpretation of a less distant CR, which would in turn imply a faster bar pattern speed. Further support for this interpretation comes from Athanassoula [1988, Fig. 4(a)]. The models with rapid pattern speeds resemble NGC 4314 more closely than do the slow pattern models.

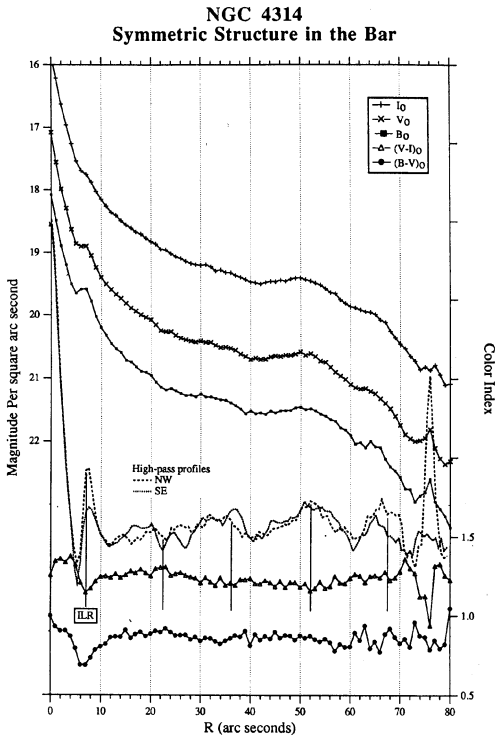

FIG. 27. Average surface-brightness and color index profiles at P.A. = 148° (along the bar) plotted with folded profiles from BVI_{hp}. The latter profiles are marked to indicate the symmetrical structures. The lack of significant color change suggests that the clumpings are due to stellar distribution variations rather than variable extinction from dust.

9.2 Star Formation in the Nuclear Ring

Following GB II and Combes (1988) we have identified the nuclear ring with an outer ILR. As Teuben *et al.* (1986) point out, a circular rotation of gas is expected within the outer ILR as the gas follows the x_2 family of orbits. These orbits are circular near the nucleus and, if elongated at all, are elongated perpendicular to the bar. In the bar between the ILR and CR, one expects the gas to follow the x_1 family, elongated along the bar. We have noted that the gas in the dust lanes exterior to the ring has significant velocity differences (points 4 and 6 in Fig. 26) compared to the ring velocity. In other words the GB I spectra at these locations have two peaks. If a parcel of gas experiences a transition from the x_1 to the x_2 family (this is an abrupt change in speed but not direction since at the ring the lanes are tangent to the ring), it seems reasonable to expect a shock. Here is a possible trigger for star formation at the nuclear ring.

9.3 The Stars in the Nuclear Spiral

The photometric characteristics of the stars in the nuclear spiral could provide us with crucial information concerning the star formation and redistribution processes within NGC 4314. The μ_{V-I}, μ_{I-J}, and μ_{B-H} maps (Fig. 7) and the BVI_{hp} and I_{hp} maps (Figs. 17 and 18) force us to conclude that a pattern of newer stars exists, strongest at the ring and almost disappearing as it reaches the linear dust lanes. We

have determined shape parameters and orientation for this spiral (or ellipse) in Sec. *8.3*. It is equally clear that all the new star formation takes place within the boundaries of the nuclear ring. We see no spiral just outside the ring in 6 cm radio continuum (GB II) or Hα (Pogge 1989). Similarly, μ_{B-H} indicates *newer* stars but no regions of *new* star formation in the spiral pattern external to the nuclear ring.

In Sec. *8.4* we derived parameters describing the spheroidal component. We drew attention (Fig. 26) to the excess signal above the spheroid in all bandpasses. This excess is exactly coincident with the nuclear spiral (or ellipse) pattern. Ideally, one would like to remove the effects of the spheroid to determine the intrinsic color properties of these stars. Intrinsic colors would provide age information. If these stars are very blue (young), then they must have formed very near their present locations. Unfortunately, the spheroidal parameters obtained (Fig. 26) are too uncertain and the S/N too low at these magnitude levels with these data. A satisfactory subtraction of the spheroid must await high-resolution mapping, so that the bar/spheroidal contribution nearest to the newer stars can be identified and thereby more accurately removed. For this study, we can only say that the stars in the nuclear spiral are bluer than the bar and spheroid. They are, thus, more recently formed stars.

How is the newer stellar material just exterior to the nuclear ring produced? How do these newer stars get to these positions? We discuss several possibilities: (1) a spiral potential (e.g., M51), which causes new star formation with a spiral shape; (2) stellar dynamics, which redistributes the newly formed stars from the ring into an ellipse, (3) gas dynamics, which arranges masking dust in a spiral pattern; or (4) a nuclear bar potential, which drives a spiral pattern.

Do spiral formation scenarios predict what we see in NGC 4314? These observations do not support a standard spiral potential genesis for the nuclear spiral. If one invokes a standard spiral density wave star formation process, the newest stars should be associated with the leading edge of the dust lanes (compare GB II 6 cm with μ_{I-J}) as in M51. We see star formation only at the ring, not exterior to the ring. There is no evidence from Hα (Pogge 1989) or radio continuum observations (GB II) for star formation associated with the nuclear spiral exterior to the nuclear ring. To preserve star formation engendered by a density wave, we must then accept that we are observing NGC 4314 at a special time, when stars formation is not occurring along most of the length of the nuclear spiral.

Can stellar dynamics explain the distribution? The dynamics of stars in barred potentials allow for the outward movement of stars from an inner ring to an ellipse. What orbits would stars newly formed in the nuclear ring follow? Teuben & Sanders (1985) describe the possible orbit families:

x_1 *family*. Prograde orbits, constrained to lie within the bar, and highly elongated. Such an orbit would take newer stars to points exterior to the ring only in the direction of the long axis of the bar.

x_2 *family*. Prograde orbits, perpendicular to the bar, and exist only between the inner ILR and outer ILR, in range $1 \leqslant r \leqslant 7$ arcsec. These orbits cannot carry a star to a point outside the outer ILR.

x_4 *family*. Stable retrograde orbits, mildly elongated, and perpendicular to the bar near the nucleus. These orbits could take stars away from the ring and in a direction perpendicular to the bar.

If the stars are not formed at their present location by a spiral density wave, the observations require that a star newly formed in the CO ring travel outward from the ring. Any set of orbits will permit stars, once formed, to move away from the ring. Only the x_4 orbits permit stars to trail or fall behind the formation sites and to move to locations outside the outer ILR, perpendicular to the bar. From Sec. *8.3* we recall that the ellipse fit to the newer stars had P.A. = 49°, a value close to the bar perpendicular (P.A. = 58°) that is required by the x_4 family.

However, there are several major difficulties with assigning these newer stars to the x_4 family. Why don't new stars, formed at formation sites perpendicular to the bar (to the SW and NE), cross the nuclear ring? In other words, why are there no new stars interior to the nuclear ring? Also, the required flip in the angular momentum vector, from prograde orbits for the gas forming the star, to retrograde orbits for the formed stars, is difficult to explain.

Can masking dust explain the nuclear spiral? Dust controls the morphology of the nuclear region a strongly as sites of new star formation. To a certain extent dust shapes the visual appearance of the bar. We now explore the possibility that the nuclear spiral could be a rather uniform distribution of newer stars delineated by dust. To produce a spiral dust pattern, Combes (1988) discusses cloud–cloud collisions, equivalent to a viscosity, which cause the gas streaming lines to gradually change their orientations by 90° between two resonances. Hence, between the outer ILR and CR, this orientation change mimics a spiral (see Combes 1988, Fig. 7). This process, called orbit and orbit orientation crowding, is also discussed in Kenney & Lord (1991). It is a way to distribute dust in a spiral pattern.

Structural features close to the nuclear ring include the spiral-shaped flux deficits seen in I_{hp} and J_{hp} (Fig. 18). The arcs in I_{hp} are coincident with the small amounts of reddening seen in μ_{I-J} and μ_{V-I} (Fig. 7) outboard from the ring, and therefore can be attributed to weak dust concentrations. Supporting a dust genesis, the I_{hp} deficit arcs do connect to dust interior to the ring at P.A. = 0° and 180°. This latter state of affairs argues against the possibility that these I_{hp} arcs are a "ringing" phenomena, similar to the holes surrounding the bright stars (see Fig. 17).

Other arcs outside the nuclear spiral (seen in J_{hp} at greater radial distances than the I_{hp} arcs), are also spiral-shaped flux deficits. They *also* connect to the dust lanes on the leading edges of the bar. This, and the coincidence with strong CO signals [compare Figs. 18(d) and 26], persuade us to interpret the arcs as dust. In contrast we see no associated variations in either μ_{V-I} or μ_{I-J}, which argues against dust. However, these are less than 3% perturbations to the smooth background. Given the noise levels in the color index maps, we might not detect color changes of 0.03 mag. If they are dust, why are they not redder in, say, μ_{V-I} or in μ_{I-J}? We suggest scattering (Thronson *et al.* 1990).

In conclusion, since we detect dust on both the interior and exterior sides of the spiral, masking must have some effect. However, invoking masking dust does not explain the required underlying uniform distribution of newer stars.

Finally, the SWIR data suggest the presence of a nuclear bar (Fig. 9). As another possibility, we suggest that the nuclear spiral might be formed and sustained by the nuclear bar. The nuclear region is then a scaled-down version of the standard bar-driven spiral discussed in, for example, Combes & Gerin (1985).

It may be that all these processes or some combination have a hand in determining the nuclear morphology of NGC 4314. Additional observations will be required to disentangle these possible causative agents.

10. DISCUSSION

In the following we will bring together all of the identified structural elements of the nuclear environment into a schematic diagram. With this overview in place we will then compare NGC 4314 to NGC 1097, a galaxy superficially similar. Lastly, we lay out a possible mechanism for star formation within NGC 4314.

10.1 The Nuclear Region—A Schematic Diagram

In an attempt to tie together the many pieces of observational evidence concerning star formation in the nucleus, we present a schematic diagram of NGC 4314 overlaid on a μ_{B-H} color index map (Fig. 28). On this schematic we have placed:

(a) The best-fit spiral (Sec. *8.3*) which matches the μ_{B-H} distribution of newer stars external to the nuclear ring. We also display an ellipse fit to this same distribution, representing the x_4 family of orbits. The ellipse fit produced a major axis P.A. = 48°, nearly perpendicular to the bar axis, as required for the x_4 family.

(b) The dust lanes on the leading edge of the bar, best seen in μ_{V-I} (Fig. 5) and BVI_{hp} (Fig. 17). At the ring, the lanes are nearly tangent to the ring and are fairly linear. The CO velocity components inferred from GB II suggest that gas associated with the dust is moving in toward the nuclear ring along these lanes.

(c) The location ($x = -9, y = -15$ arcsec) of the stars assumed to be unreddened that were used to determine the near-nuclear ring A_V values in Sec. *7.3*,

(d) The dust arcs from J_{hp} [Fig. 18(d)]. The two arcs are pieces of the spiral fit in Sec. *8.3*, but rotated 90° clockwise. The role this dust plays in star formation is unclear. We include these arcs on the schematic for the sake of completeness.

(e) A contour of constant rotational velocity ($V = 124$ km/s), which assumes an inclination $i = 30°$ (WN) and a dynamical line of nodes at P.A. = 135°. This ellipse matches the distribution of H II regions. It represents the CO ring postulated by GB II.

(f) The paths and orientations of the detailed luminosity and color profiles of Figs. 14(a) and 14(b).

The stellar and dust spirals have identical pitch angles. Note that the stellar spiral intersects the P.A. = 58° profile at $r = 10.5$ arcsec, precisely where the excess over the modeled bulge occurs in Fig. 25. Thus, we detect the nuclear spiral, even in *K*, supporting the claim that the nuclear spiral or x_4 locus is a stellar component of the galaxy.

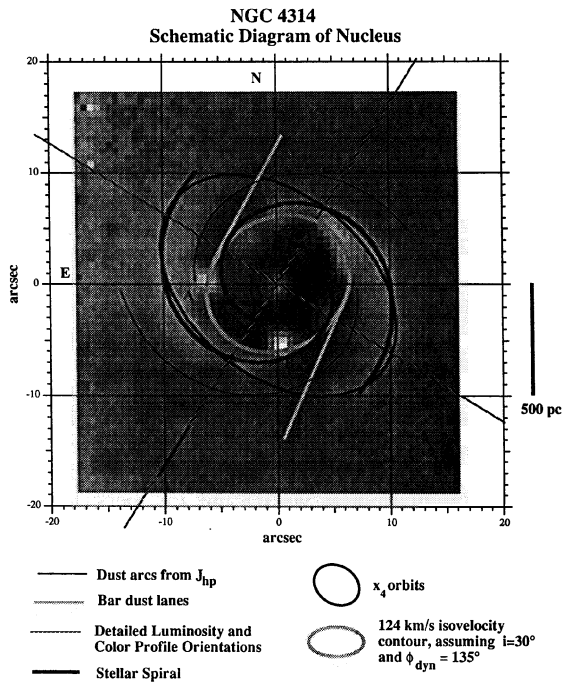

FIG. 28. Various components of NGC 4314 overlaid on a μ_{B-H} map. The grid is in arcsec from the center. These components include (a) the spiral and ellipse (x_4 orbits) fits to the newer stars exterior to the nuclear ring, (b) the "linear" dust lanes along the bar leading edge, (c) the location ($x = -9$, $y = -15$ arcsec, or R.A. = $12^h\ 22^m\ 32.7^s$, Dec. = $+29°\ 53'\ 30''$) of the stars assumed to be unreddened and used to determine the ring A_V in Sec. *7.3*, (d) the spiral locus of deficit seen in J_{hp}, and (e) the $V = 124$ km s^{-1} isovelocity contour for $i = 30°$, $\phi = 135°$, representing the CO ring, (f) the detailed luminosity and color index profile orientations for Fig. 14. We also identify knots A and B from WN.

10.2 Comparison with NGC 1097

The structure of NGC 4314 is in many ways similar to that of NGC 1097. They both contain a nuclear ring prominent in Hα, 6 cm, 20 cm, and CO. Both contain dust lanes in the bar and have dust interior to the ring (Hummel *et al.* 1987, Gerin *et al.* 1988). However, NGC 1097 is H I rich; NGC 4314 is H I poor (GB II). Given the anemic classification of NGC 4314 can we interpret NGC 1097 as being a gas-rich version of the same basic galaxy?

The dust lanes in the bar are detected at 20 cm in NGC 1097, but not in NGC 4314. The nuclear ring is over twice the physical size in NGC 1097. Also, the nucleus of NGC 1097 is experiencing star formation, while that of NGC 4314 is not. NGC 1097 is also IR active, being classified as an AGN (Telesco 1988). NGC 1097 has no obvious nuclear spiral structure external to the nuclear ring in the μ_{B-V} map of Hummel *et al.* (1987) or in the color picture of Wray (1988). The dust lanes in the bar of NGC 1097 extend all the way to the bar ends. Those in NGC 4314 end midway out the bar. There is some star formation near the bar dust lanes in NGC 1097 (Wray 1988), but none in or near the bar dust in NGC 4314.

While some of the differences might be ascribed to total gas content, NGC 1097 is not just a raw-material rich version of NGC 4314. The differing bar dust lane morphologies, the lack of a nuclear spiral, and an AGN in NGC 1097 argue that different sets of resonances prevail in the two galaxies. Hence, the bar pattern speed and/or the overall mass distribution must differ.

10.3 The Star Formation Engine

With our schematic in hand (Fig. 28) and an appreciation for the uniqueness of this galaxy we wish to now discuss the star formation engine in NGC 4314. The basic structure of interest is an inner CO and dust ring that is coplanar with the galaxy disk. This ring has a projected $V_{\rm rot} \approx 120$ km s^{-1} (WN). We next assume that the dust within the bar is coplanar with the disk. We know that massive star formation is confined to a ring and that star production is episodic, because the ring is not uniformly packed with new stars. And, we have seen that the spiral or ellipse just external to the ring contains stars younger than the bar and disk.

Suppose that star formation is instigated at the intersection of the rotating CO ring and the gas moving inward within the dust lanes along the leading edge of the bar. The CO measurements of GB suggest that the dust velocity within the bar is $V_{\rm dust} \approx 90$ km s^{-1}. Hence, the impact occurs at about 30 km s^{-1}. Once shocked, the gas continues to share the ring kinematics *until the stars are formed.* Variable delays between shock and star formation will distribute new stars randomly around the ring. We assume that the lifetime of H II region stars is about $t = 3$ My. This mechanism explains why the newest stars and the H II regions are confined to the ring with $r = 6$ arcsec.

As mentioned before, the formation process is not continuous, since the ring is not continuous in Hα, radio continuum, or μ_{B-H}. If the nuclear spiral arms are somehow related to the ring of star formation we might expect them to contain gaps, and they do, as can be seen in Figs. 17 and 18(b). Their exact relationship with the nuclear ring remains a puzzle.

11. SUMMARY

Some major results of this study have included mapping the distribution of the old stellar population in the nucleus and the discovery of an inner bar seen only in the SWIR data.

We have detected a stellar nuclear spiral just exterior to the nuclear ring in the visible and SWIR, and have mapped spiral-shaped gaps in the stellar distribution in the SWIR. The coincidence of these gaps with CO from GB II argue that they are due to dust. The nuclear ring and associated just have been detected in all SWIR color indices. We see no evidence for an underlying spiral density wave in the old stellar population at the present location of star formation, that is, at the nuclear ring.

We have determined the extinction characteristics of the dust in the bar and have determined the extinction and scattering characteristics of the dust near the sites of present-day star formation in the nuclear ring. Within the errors, the dust in NGC 4314 has similar characteristics to dust in our Galaxy and NGC 4594. We have also determined that μ_{I-J} best delineates dust. Shorter wavelengths are subject to scattering. Longer wavelengths are relatively unaffected by dust. We point out how similar the dust distribution in the bar is to the gas streamlines described in the models of Roberts *et al.* (1979).

The average minor-axis profiles show that this galaxy has a nuclear bulge obeying the de Vaucouleurs $r^{1/4}$ law in the range $2 < r < 7$ arcsec.

Surface photometry has detected structure in the bar identifiable with that predicted by theory (Teuben & Sanders 1985). We showed that simple resolution and contrast enhancement procedures provide useful clues to the dynamics of barred stellar systems. Dust lanes terminate long before the end of the outer bar and long before the bar connects with the outer spiral structure. Although dust lanes generally end or turn at CR (Combes 1988), this may not be the case for this galaxy.

Preliminary examination of the GB CO velocity field yields noncircular streaming motions for dust lanes in the bar. All photometric evidence indicates that star formation occurs only in the nuclear ring, which we identify as an outer inner Lindblad resonance. The star-forming engine in NGC 4314 consists of shocks at the intersection of dust streaming inward along the bar and the more rapidly rotating CO nuclear ring. The distribution of newer stars exterior to the nuclear ring remains an open issue because no one explanation satisfies all the observational evidence.

12. FUTURE WORK

We have many puzzles left to resolve. *I*-band HST Planetary Camera exposures are scheduled for 1991. These observations should yield 0.2 arcsec resolution. Simple enhancement techniques can remove some of the effects of spherical aberration so that shapes can be studied. These data would allow us to map the dust associated with the nuclear ring in high resolution. It may also be possible to test for the existence of an inner ILR. We will report on these observations in Paper II.

High spatial and velocity resolution CO observations are required to study gas streaming, and to permit a detailed study of the dynamics of the bar dust lanes and their interaction with the nuclear ring. These observations, obtained with the OVRO interferometer, are in the reduction and analysis phase and will appear as Paper III. We expect these observations to provide new insight into the star formation process in the nucleus of NGC 4314.

Additional SWIR surface photometry is needed to further explore the dust conditions in the bar. We would also like to confirm the N-S nuclear bar. We hope to obtain these data in conditions of excellent seeing with a wider field-of-view camera and longer exposures for a higher resulting S/N.

UBVI Guaranteed Time Observations are scheduled with the Hubble Space Telescope, using WF/PC II. These observations are unlikely to be secured before 1994, but should permit an unambiguous identification of the underlying bar and spheroidal component, as well as a more detailed examination of the star formation process.

Nearer term, *BVI* wide-field CCD photometry will be obtained to photometrically characterize the larger-scale components—the disk and the outer arms.

Finally, a radial velocity measurement of source No. 5 in Table 1 could determine the likelihood of its association with NGC 4314. If it is a part of the galaxy, it would allow the rotation curve to be extended to much larger values of the radius. Alternatively, if it is a background QSO, then one could use it to probe the gas characteristics of NGC 4314.

We thank Ron Buta for many enlightening discussions, Beverly Smith and Jeffrey Achtermann for critical readings of the manuscript, and Don Taylor and Marty Harris for help with CRT screen photography and print production. We thank Gerard de Vaucouleurs for pre-publication access to the Third Reference Catalog of Bright Galaxies. Thanks to M. Frueh for obtaining the RCA CCD galaxy frames and calibration material. An anonymous referee brought to our attention the previously known flat nature of the bar.

We used many tool/computer combinations in the reduction, analysis, and preparation of this paper. Our preliminary reductions used IDL/MicroVax. Much of the map analysis was carried out on IRAF/SUN (developed by NOAO) and AIPS/SUN (developed by NRAO). Profile analysis and paper preparation relied heavily on Wavemetrics IGOR/Macintosh and Microsoft Word/Macintosh. The annotated maps (Figs. 24, 27, and 31) were produced using a combination of NIH Image, NCSA/Spyglass View, and Canvas on a Macintosh.

Benedict and Higdon acknowledge NASA support under Contracts Nos. NAS5-29285 and NAS8-32906. Harvey, Tollestrup and Hahn acknowledge Air Force Grant No. AFOSR-86-0083.

APPENDIX: OBJECT NO. 5

What is the faint blue object at the end of the bar to the NW at $r = 76$ arcsec, also visible in a B photograph in Elmegreen (1981)? While not particularly obvious visually, it lies in a region often associated with star formation within a barred galaxy, the end of the bar (NGC 1300 being a classic example). The object lies on a sloping background, rendering background corrected photometry difficult. Despite this, we determined the background from an annulus surrounding and close to the object and obtained integrated magnitude and colors $B = 19.56$, $B - V = 0.44$, and $V - I = -0.11$. Note, too, from the major-axis profile [Fig. 16(a)], that even those colors that are uncorrected for local background are still far bluer than those of the nuclear H II regions. If object No. 5 is a H II region, it is somewhat reddened compared to Tarrab's (1982) values for Orion.

The above colors suggest newly formed stars. Therefore, on 18 April 1991, we obtained a new CCD image of this field through a Hα filter ($\lambda = 659.6$ nm, $\Delta\lambda_{1/2} = 5.7$ nm). We used the McDonald 0.8 m and the integration time was 25 m. We failed to detect the object, but easily detected knots A and B in the nuclear ring. It is evidently not a H II region associated with NGC 4314. A low-dispersion classification spectrum would be most interesting.

REFERENCES

Adamson, A. J., Adams, D. J., & Warwick, R. S. 1987, MNRAS, 224, 367
Athanassoula, E. 1988, Proceedings of the Joint Varenna-Abastumani International School and Workshop on Plasma Astrophysics, ESA SP-285, Vol. 1, p. 341
Athanassoula, E., Morin, S., Wozniak, H., Puy, D., Pierce, M. J., Lombard, J., & Bosma, A. 1990, MNRAS, 245, 130
Benedict, G. F., & Shelus, P. J. 1978, in IAU Colloquium No. 48 on Modern Astrometry, edited by F. Prochazka and R. Turner (University Observatory, Vienna), p. 295
Baumgart, C. W., & Peterson, C. J. 1986, PASP, 98, 56
Benedict, G. F. 1976, AJ, 81, 799
Benedict, G. F. 1980, AJ, 85, 513
Benedict, G. F. 1982, AJ, 87, 76
Boroson, T. A., & Thompson, I. B. 1987, AJ, 92, 33
Bosma, A. 1990, Morphological and Physical Classification of Galaxies, OAC 5th International Workshop, preprint
Bothun, G. D., & Gregg, M. D. 1990, ApJ, 350, 73
Bothun, G. D., Romanishin, W., Strom, S. E., & Strom, K. M. 1984, AJ, 89, 1300
Brosch, N., Greenberg, J. M., & Grosbol, P. J. 1985, A&A, 143, 399
Burstein, D., & Heiles, C. 1984, ApJS, 54, 33
Buta, R. 1986, ApJS, 61, 631
Campbell, A. W., & Terlevich, R. 1984, MNRAS, 211, 15
Capaccioli, M. 1989, The World of Galaxies, edited by H. Corwin and L. Bottinelli (Springer, Berlin), p. 208
Carico, D. P., Sanders, D. B., Soifer, B. T., Matthews, K., & Neugebauer, G. 1990, AJ, 100, 70
Combes, F. 1988, in Galactic and Extragalactic Star Formation, edited by E. Pudritz and M. Ficks (Kluwer, Dordrecht), p. 475
Combes, F., & Gerin, A. 1985, A&A, 150, 327
Dickman, R. L. 1988, in Molecular Clouds in the Milky Way and External Galaxies, edited by R. Dickman, R. Snell, and J. Young (Springer, Berlin), p. 55
Dressel, L. L., Telesco, C. M., & Decher, R. 1990, in Dynamics and Interactions of Galaxies, edited by R. Wielen (Springer, Berlin), p. 488
Elias, J. H., Frogel, J. A., Matthews, K., & Neugebauer, G. 1982, AJ, 87, 1029
Elmegreen, D. M. 1981, ApJS, 47, 229
Elmegreen, B. G., & Elmegreen, D. M. 1985, ApJ, 288, 438
Frogel, J. 1985, ApJ, 298, 528
Garcia-Barreto, J. A., Combes, F., & Magri, C. 1989, The World of Galaxies, edited by H. Corwin and L. Bottinelli (Springer, Berlin), p. 387 (GB I)
Garcia-Barreto, J. A., Downes, D., Combes, F., Gerin, M., Magri, C., Carrasco, L., & Cruz-Gonzalez, I. 1991, A&A, 244, 257 (GB II)
Gerin, M., Nakai, N., & Combes, F. 1988, A&A, 203, 44
Grosbol, P. J. 1985, A&AS, 60, 261
Hummel, E., van de Hulst, J. M., & Keel, W. C. 1987, A&A, 172, 32
Hutchings, J. B., Neff, S. G., Stanford, S. A., Lo, E., & Unger, S. W. 1990, AJ, 100, 60
Joy, M., Ellis, H. B., Tollestrup, E. V., Brock, D., Higdon, J. L., & Harvey, P. M. 1988, ApJ, 330, L29
Kenney, J. D. P., & Lord, S. D. 1991, ApJ, 381, 118
Koornneef, J. 1983, A&A, 128, 84
Knapen, J. H., Hes, R., Beckman, J. E., & Peletier, R. F. 1991, A&A, 241, 42
Landolt, A. U. 1983, AJ, 88, 439
Laustsen, S., Madsen, C., & West, R. 1987, Exploring the Southern Sky (Springer, Berlin), p. 39
Lequeux, J. 1990, in Evolution of Galaxies, Astronomical Observations, edited by I. Appenzeller, H. Habing, and P. Lena (Springer, Berlin), p. 149
Lynds, B. T., Furenlid, I., & Rubin, J. 1973, ApJ, 182, 659
Mould J., Graham, J., Matthews, K., & Soifer, B. T. 1989, ApJ, 339, L21
Peletier, R. F., Valentijn, E. A., & Jameson, R. F. 1990, A&A, 233, 62
Pence, W. D., & Blackman, C. P. 1984, MNRAS, 207, 9
Persson, S. E., Aronson, M., Cohen, J. G., Frogel, J. A., & Matthews, K. 1983, ApJ, 266, 105
Pogge, R. W. 1989, ApJS, 71, 433
Roberts, W. W., Huntley, J. M., & van Albada, G. D. 1979, ApJ, 233, 67
Rosenfeld, A., & Weszka, J. S. 1976, Computer, 9, 28
Sandage, A. R. 1961, The Hubble Atlas of Galaxies (Carnegie Institute of Washington, Washington, DC), Publ. 618
Savage, B., & Mathis, J. 1979, ARA&A, 17, 73
Scheffler, H., & Elsasser, H. 1987, Physics of the Galaxy and Interstellar Medium (Springer, Berlin)
Schild, R. E. 1983, PASP, 95, 1021
Schombert, J. M., & Bothun, G. D. 1987, AJ, 93, 60
Shlosman, I., Begelman, M. C., & Frank, J. 1990, Nature, 345, 679
Soifer, B. T., Boehmer, L., Neugebauer, G., & Sanders, D. B. 1989, AJ, 98, 766
Tarrab, I. 1982, A&A, 113, 57
Telesco, C. M. 1988, ARA&A, 26, 343

Telesco, C. M., & Gatley, I. 1984, ApJ, 284, 557
Telesco, C. M., Gatley, I., & Stewart, J. M. 1982, ApJ, 263, L13
Teuben, P. J., & Sanders, R. H. 1985, MNRAS, 212, 257
Teuben, P. J., Sanders, R. H., Atherton, P. D., & van Albada, G. D. 1986, MNRAS, 221,1
Thronson, H. A., Majewski, S., Descartes, L., & Hereld, M. 1990, ApJ, 364, 456
Tilanus, R., Allen, R., van der Hulst, J., Crane, P., & Kennicutt, R. 1988, ApJ, 330, 667
Tubbs, A. D. 1982, ApJ, 255, 458
van den Bergh, S. 1976, ApJ, 206, 883
van den Bergh, S. 1991, Dominion Astrophysical Observatory preprint to appear in PASP
de Vaucouleurs, G. 1975, ApJS, 29, 193
de Vaucouleurs, G., de Vaucouleurs, A., and Corwin, H. 1976, The Second Reference Catalog of Bright Galaxies (University of Texas, Austin)
Vorontsov-Vel'yaminov, G. A., Zaitseva, G. V., & Lyuti, V. M. 1972, SvAJ, 16, 71
Vogel, S. N., Kulkarni, S. R., & Scoville, N. Z. 1988, Nature, 334, 402
Wakamatsu, K., & Nishida, M. T. 1980, PASJ, 32, 389 (WN)
Wray, J. D. 1988, The Color Atlas of Galaxies (Cambridge, London)

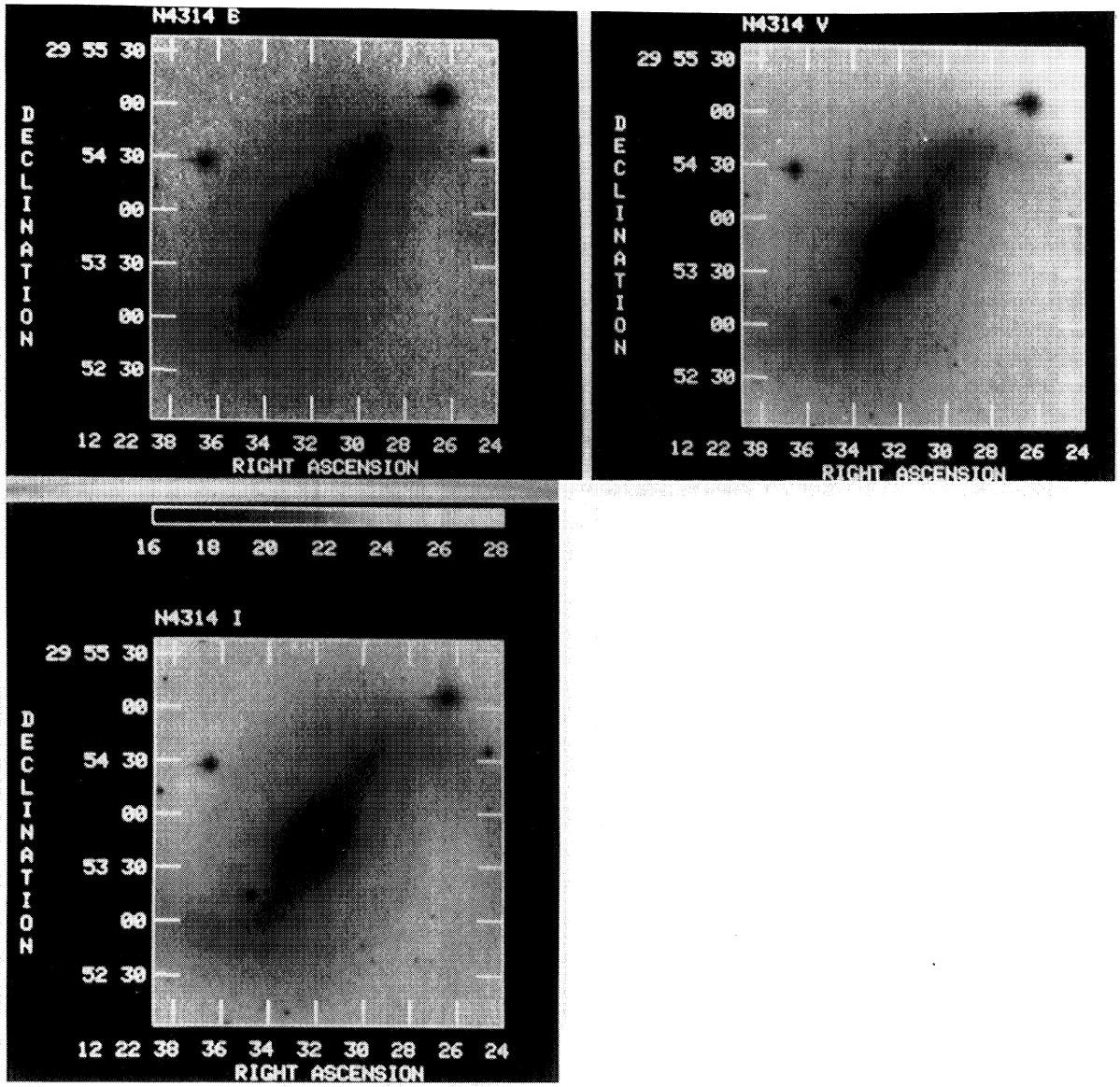

FIG. 4. Grey-scale surface magnitude maps: μ_B, μ_V, and μ_I for the outer frame.

Benedict *et al.* (see page 761)

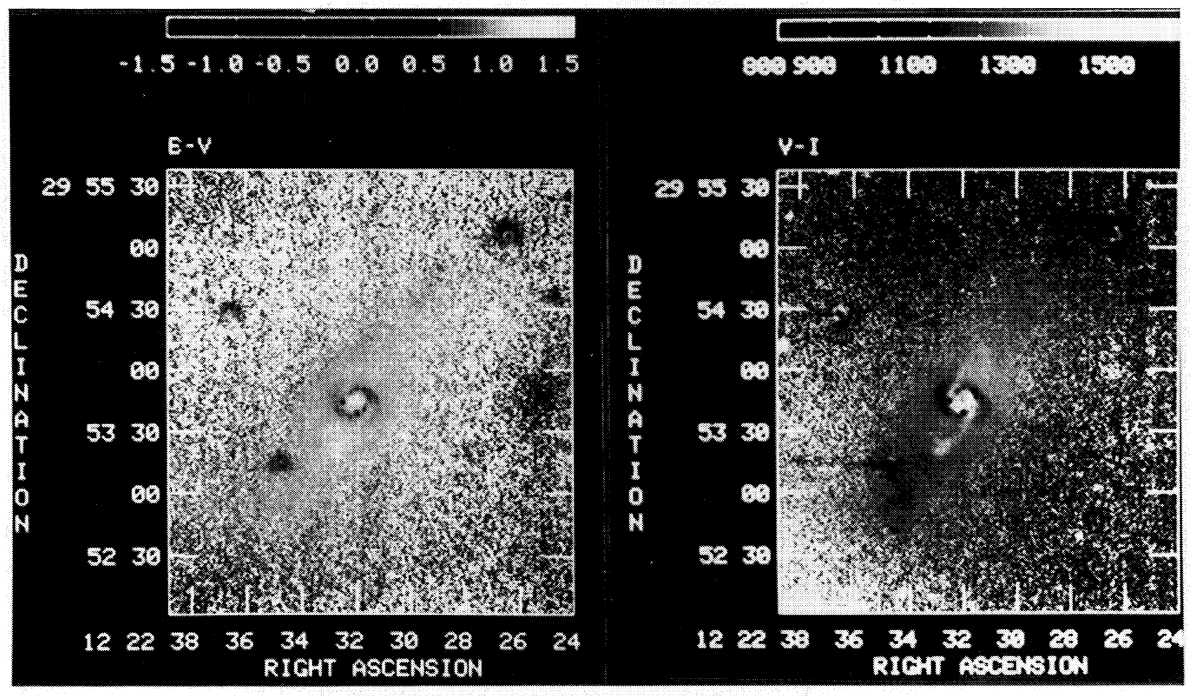

FIG. 5. Grey-scale maps: (a) μ_{B-V} and (b) μ_{V-I} for the outer frame. Scales are given in surface magnitudes for μ_{B-V} and in millimagnitudes for μ_{V-I}. Both are encoded such that redder is lighter.

Benedict *et al.* (see page 761)

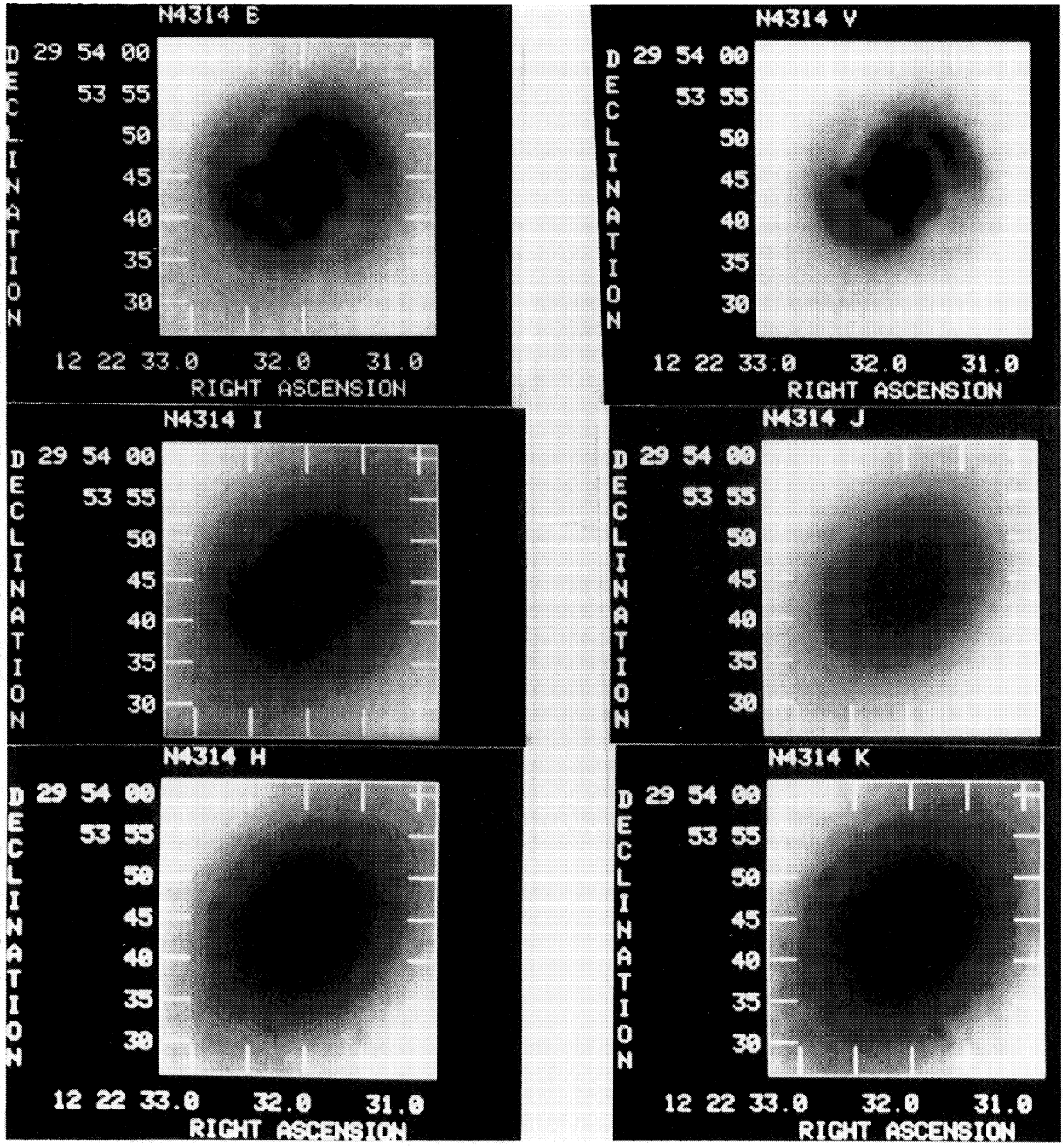

FIG. 6. *B*, *V*, *I*, *J*, *H*, and *K* grey-scale surface magnitude maps for the inner frame.

Benedict *et al.* (see page 761)

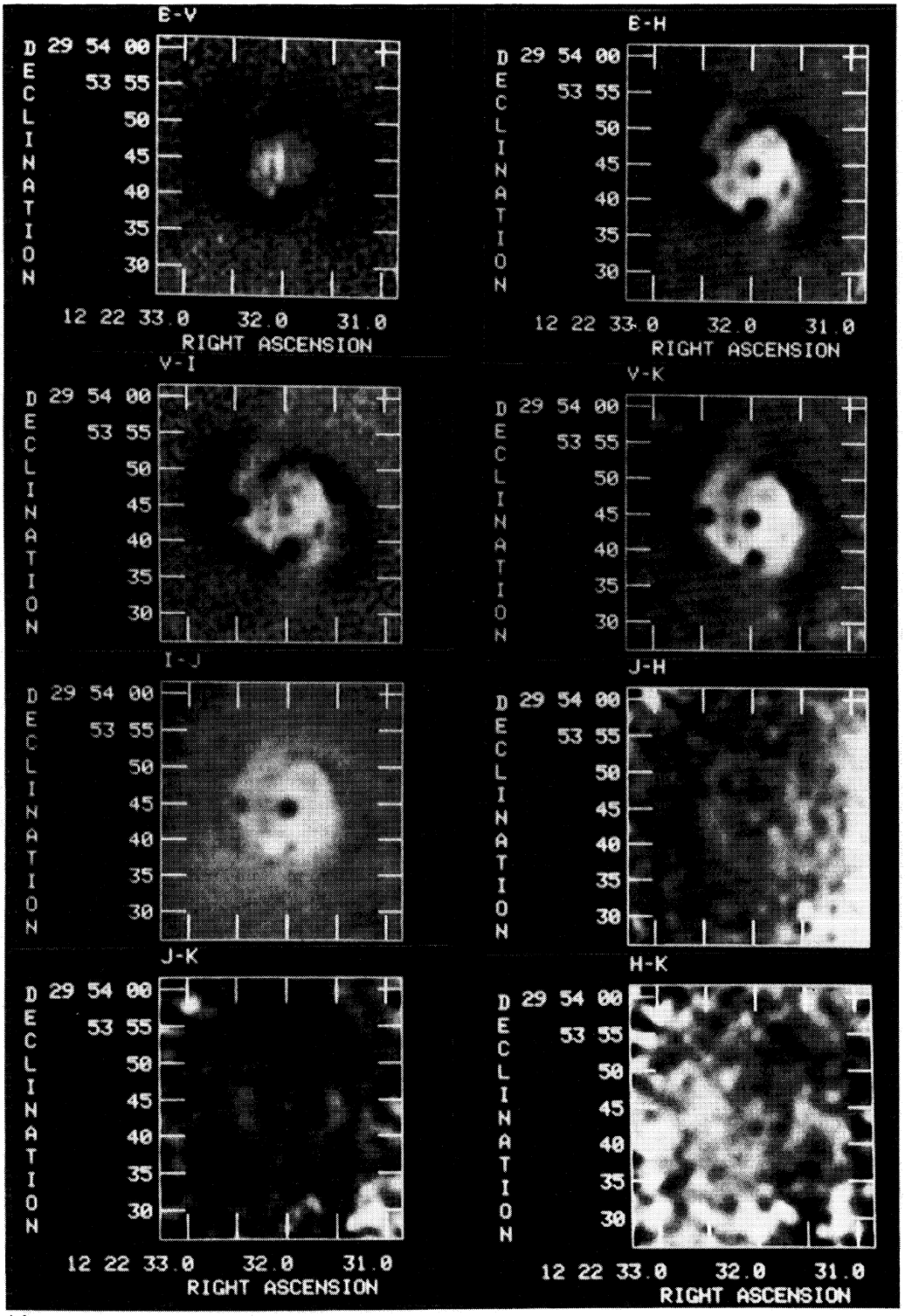

(a)

FIG. 7. Grey-scale surface color index maps for the inner frame: (a) encoded such that darker corresponds to bluer, (b) enlarged μ_{I-J} encoded such that darker corresponds to redder. The orientation is the same as for (a).

Benedict *et al.* (see page 761)

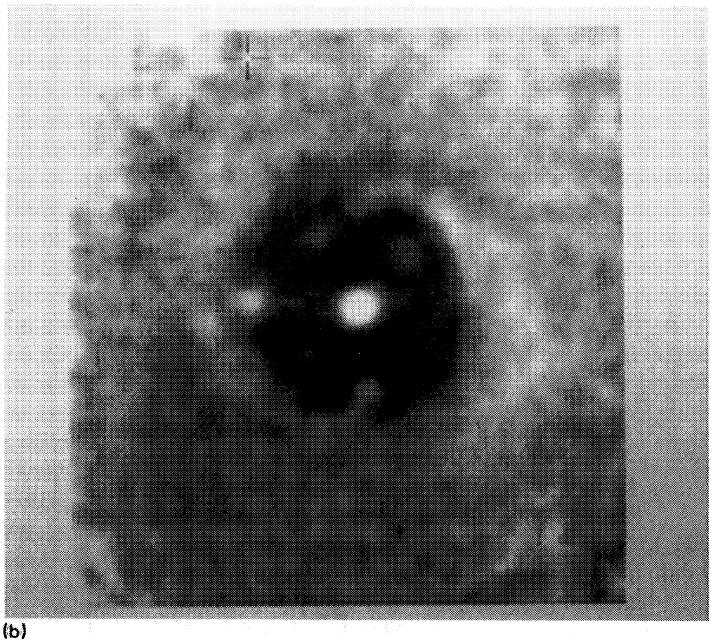

FIG. 7. (continued)

Benedict *et al.* (see page 761)

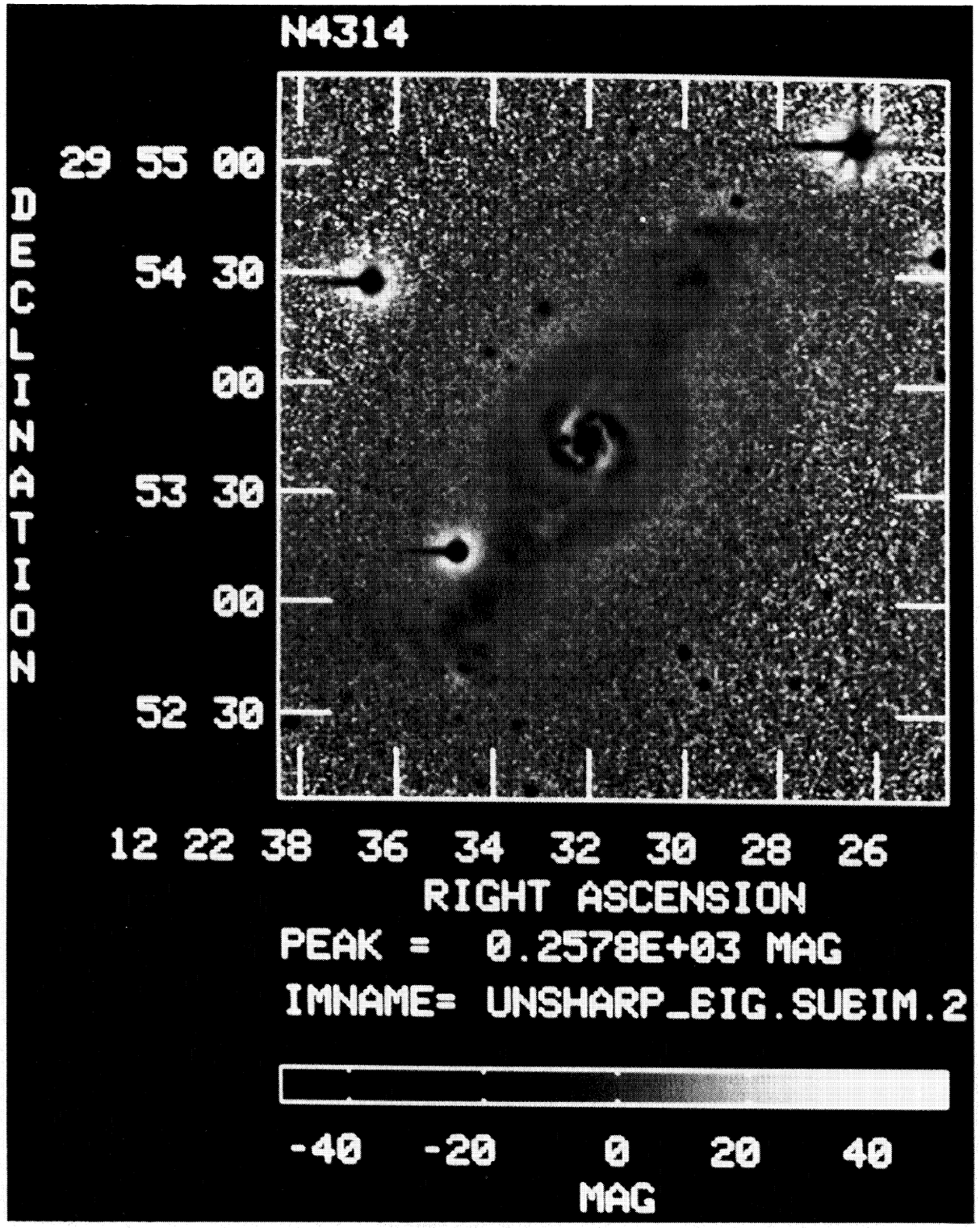

FIG. 17. A frame produced by averaging the *B*, *V*, and *I* outer frame and subjecting the result to an unsharp masking process. Encoded such that darker regions correspond to higher signal. Note the multiple condensations within the bar. The NW dust lane is clearly seen to turn and return to the vicinity of the nuclear ring. Note also the inner rings, especially to the N.

Benedict *et al.* (see page 766)

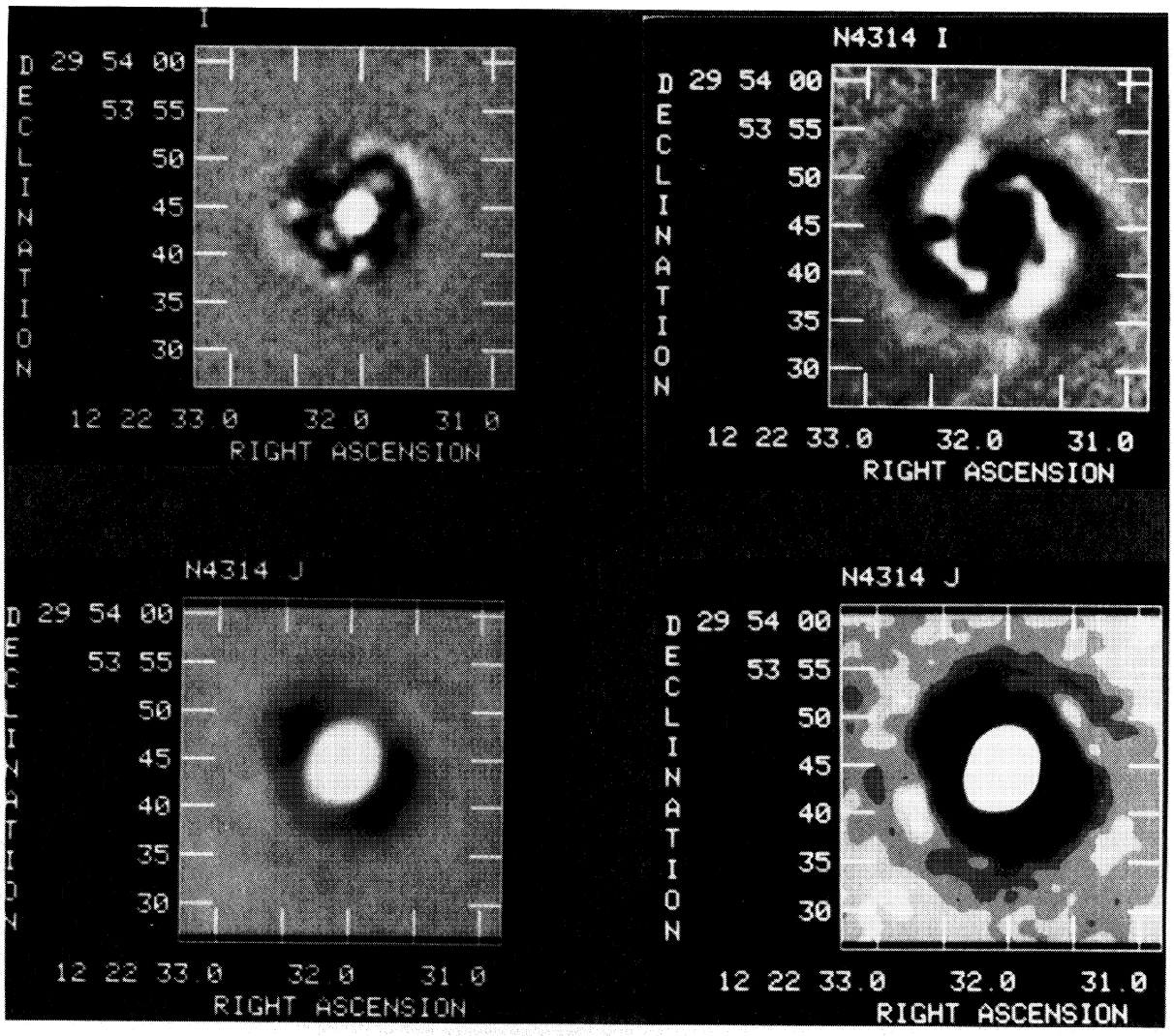

FIG. 18. Unsharp masked results for the inner frame: (a), (c), and (d) encoded such that darker regions correspond to lower signal. Clockwise from top left: (a) I_{hp}, (b) I_{hp} contrast enhanced to show the structure just exterior to the nuclear ring. Dark corresponds to higher signal for this panel, (c) J_{hp}, contrast enhanced to better show the spiral shaped arcs of lower signal just exterior to the nuclear ring, and (d) J_{hp}, normal contrast. The arcs are easily visible in (c) to the NW and SE.

Benedict *et al.* (see page 766)